nature materials

ARTICLES

https://doi.org/10.1038/s41563-021-01108-x

Microtubules tune mechanosensitive cell responses

Shailaja Seetharaman[1,2], Benoit Vianay[3], Vanessa Roca[1], Aaron J. Farrugia[4], Chiara De Pascalis[1], Batiste Boëda[1], Florent Dingli[5], Damarys Loew[5], Stéphane Vassilopoulos[6], Alexander Bershadsky[4], Manuel Théry[3] and Sandrine Etienne-Manneville[1]✉

Mechanotransduction is a process by which cells sense the mechanical properties of their surrounding environment and adapt accordingly to perform cellular functions such as adhesion, migration and differentiation. Integrin-mediated focal adhesions are major sites of mechanotransduction and their connection with the actomyosin network is crucial for mechanosensing as well as for the generation and transmission of forces onto the substrate. Despite having emerged as major regulators of cell adhesion and migration, the contribution of microtubules to mechanotransduction still remains elusive. Here, we show that talin- and actomyosin-dependent mechanosensing of substrate rigidity controls microtubule acetylation (a tubulin post-translational modification) by promoting the recruitment of α-tubulin acetyltransferase 1 (αTAT1) to focal adhesions. Microtubule acetylation tunes the mechanosensitivity of focal adhesions and Yes-associated protein (YAP) translocation. Microtubule acetylation, in turn, promotes the release of the guanine nucleotide exchange factor GEF-H1 from microtubules to activate RhoA, actomyosin contractility and traction forces. Our results reveal a fundamental crosstalk between microtubules and actin in mechanotransduction that contributes to mechanosensitive cell adhesion and migration.

Cells sense the physical properties of their environment, translate them into biochemical signals and adapt their behaviour accordingly. This process, known as mechanotransduction, is crucial during development and in the adult, during physiological and pathological conditions such as cell migration, wound healing and cancer[1,2]. Integrin-mediated focal adhesions (FAs) sense the matrix rigidity, control the generation of actomyosin-dependent forces and the transmission of these traction forces onto the substrate; FAs also contribute to mechanosensitive cell responses such as migration[3,4]. In addition to the actin cytoskeleton, microtubules are also key regulators of two- and three-dimensional cell migration[5–8]. Several studies have demonstrated the role of the actomyosin cytoskeleton and FAs in mechanotransduction; however, very little is known about microtubules in this context. In this study, we used primary rat astrocytes and primary human umbilical vein endothelial cells (HUVECs; both types of cells are dependent on efficient microtubule dynamics for migration or invasion[9–13]) to address the role of microtubules in rigidity sensing and mechanosensitive migration.

The crucial factors affecting the functions of the microtubule network are post-translational modifications (PTMs) of tubulin, such as acetylation, which occurs at the K40 residue of α-tubulin. The enzyme responsible for microtubule acetylation, α-tubulin acetyltransferase 1 (αTAT1, also known as MEC-17), is present in the lumen of microtubules[14] and is highly specific to α-tubulin K40. On the other hand, the enzymes involved in deacetylation at K40 are histone deacetylase family member 6 (HDAC6) and sirtuin type 2 (Sirt2), both of which target other substrates as well[15]. In this study, we used previously characterized short interfering RNAs (siRNAs) that target αTAT1 (set 1: siαTAT1-1; set 2: siαTAT1-2; ref. [13]; Extended Data Fig. 1a–c) to decrease acetylation, and Tubacin (Extended Data Fig. 1a,c), a drug that increases microtubule acetylation by inhibiting HDAC6 without modifying the acetylation of other HDAC6 substrates such as histones[16,17].

Substrate rigidity promotes microtubule acetylation through integrin β_1 signalling

We have previously shown that microtubules come in close proximity to FAs, and that microtubule acetylation promotes FA turnover during migration[13]. Because FAs are major mechanosensitive structures[18], we investigated whether the extracellular matrix rigidity affects microtubule acetylation. Astrocytes were plated sparsely on polyacrylamide (PAA) hydrogels of different rigidities: 1.26, 2, 9 and 48 kPa (Fig. 1a,b). The astrocytes on soft substrates exhibited lower levels of acetylated tubulin than cells on stiff substrates (Fig. 1a,b). Tubulin acetylation levels showed a twofold increase with increasing rigidity (1.26–48 kPa), a highly significant change in comparison with the maximal 3.8-fold increase obtained after Tubacin treatment (Extended Data Fig. 1d). Subsequently, to determine whether microtubule acetylation may be indirectly caused by a mechanism involving differential cell spreading, we plated astrocytes on adhesive micropatterns (area 2,500 μm^2) printed on 2 and 40 kPa hydrogels (Extended Data Fig. 1e). Similar to stiff substrates, the astrocytes on soft substrates adopted a crossbow shape and identical spread area, and yet, microtubule acetylation increased on stiff substrates compared with on softer substrates (Extended Data Fig. 1e). In contrast to tubulin acetylation, tubulin detyrosination (another tubulin PTM) remained unaffected by increased substrate rigidity in astrocytes (Extended Data Fig. 1f,g), and had no affect on astrocyte adhesion

[1]Cell Polarity, Migration and Cancer Unit, Institut Pasteur, UMR3691 CNRS, Equipe Labellisée Ligue Contre le Cancer, Paris, France. [2]Université Paris Descartes, Paris, France. [3]Paris University, INSERM, CEA, Hôpital Saint Louis, Institut Universitaire d'Hematologie, Paris, France. [4]Mechanobiology Institute, National University of Singapore, Singapore, Singapore. [5]PSL Research University, Centre de Recherche, Laboratoire de Spectrométrie de Masse Protéomique, Institut Curie, Paris, France. [6]Sorbonne Université, INSERM UMRS 974, Institute of Myology, Paris, France. ✉e-mail: setienne@pasteur.fr

and migration[13], suggesting that rigidity sensing specifically affects microtubule acetylation.

Integrin-based FAs sense the matrix rigidity and trigger mechanosensitive signalling pathways[19]. To determine the role of integrin signalling in controlling microtubule acetylation, we first used a scratch-induced migration assay to trigger integrin activation at the wound edge[12]. The addition of cyclic RGD (cRGD) peptide, to prevent the binding of integrins to the RGD motif of extracellular matrix proteins, reduced tubulin acetylation (Extended Data Fig. 2a). Furthermore, integrin activation using $MnCl_2$ (ref. [20]) led to an increase in microtubule acetylation as compared with control cells (Extended Data Fig. 2b). Finally, depletion of β_1 integrin using a siRNA (Extended Data Fig. 2c) also resulted in a significant decrease in tubulin acetylation as compared with control cells (Extended Data Fig. 2c,d), suggesting that β_1 integrins are major players in the control of microtubule acetylation. We then investigated the involvement of two central players in integrin signalling: the proto-oncogene c-Src and focal adhesion kinase (FAK). In migrating astrocytes, the inhibition of Src (using Src kinase inhibitor 1, referred to here as Src kin 1) and FAK (using PF-562271) drastically reduced the levels of acetylated tubulin (Extended Data Fig. 2e). In addition, following Src and FAK inhibition, microtubule acetylation induced by cell spreading on 48 kPa substrates decreased to a level similar to that observed on soft substrates (Fig. 1c and Extended Data Fig. 2f), indicating that Src and FAK are required for the rigidity-dependent increase in acetylation. Altogether, these results strongly suggest that β_1 integrin-mediated signalling promotes substrate rigidity-induced acetylation of microtubules.

αTAT1 interacts with talin in mechanosensitive manner

Microtubule acetylation is mediated by αTAT1; however, the mechanisms by which αTAT1 is recruited and/or activated remains unknown[21]. Therefore, we carried out a quantitative mass spectrometry screen to identify interacting partners of αTAT1 using HEK293 cells. The mass spectrometry data (data available from ProteomeXchange with identifier PXD015871, see Methods for details; Extended Data Fig. 2g) revealed interesting potential interactors, amongst which the proteins enriched in the gene ontology for focal adhesions, depicted in red in Extended Data Fig. 2g. One of the significant interactors identified in the mass spectrometry screen was talin (Extended Data Fig. 2g), a mechanosensitive partner of integrins[19]. We confirmed the interaction of αTAT1 with talin through pull-down experiments. GST-αTAT1, but not GST alone, associated with endogenous talin from astrocyte lysates (Fig. 1d and Extended Data Fig. 2h). The interaction was further confirmed by immunoprecipitation using GFP-αTAT1-transfected astrocytes. talin co-immunoprecipitated with GFP-αTAT1, but not with GFP alone (Fig. 1e and Extended Data Fig. 2i). In addition, using total internal reflection fluorescence (TIRF) microscopy, we observed that GFP-αTAT1 strongly localized at mCherry-vinculin-positive FAs (Fig. 1f)[13]. We then investigated whether talin played a role in the recruitment of αTAT1 to FAs and the acetylation of microtubules. Therefore, we used specific siRNAs to reduce talin expression in primary astrocytes (Extended Data Fig. 2j). Talin depletion reduced GFP-αTAT1 recruitment to FAs (Fig. 1f). In addition, talin-depleted astrocytes plated on 48 kPa substrates exhibited decreased levels of tubulin acetylation as compared with the control cells (Fig. 1g).

As αTAT1 is also present within microtubules (Extended Data Fig. 2k)[13,14], we tested whether the recruitment of αTAT1 to FAs was dependent on microtubules. To address this, GFP-αTAT1 and mCherry-vinculin expressing astrocytes were treated with nocodazole to depolymerize all microtubules. The nocodazole-treated astrocytes displayed larger adhesions and increased stress fibres, as has been observed in other cell types (Extended Data Fig. 2l and Supplementary Video 1)[22,23], and increased αTAT1 at FAs (Extended Data Fig. 2l and Supplementary Video 1), suggesting that microtubules are not required to localize αTAT1 at FAs, and that increased actomyosin contractility might facilitate αTAT1 concentration at FAs. As actomyosin contractility is required for talin-mediated mechanosensing[24,25], we used the Rho kinase (ROCK) inhibitor Y-27632 (which strongly reduces actomyosin contractility[26]) to assess its role in the mechanosensitive acetylation of microtubules. Through GST-αTAT1 pull-down as well as TIRF microscopy, we observed that Y-27632 treatment decreased the αTAT1 interaction with talin (Fig. 1h,i and Supplementary Video 2) and tubulin acetylation (Fig. 1j,k), confirming that actomyosin contractility and mechanosensing at FAs influence microtubule acetylation. Altogether, these results suggest that talin- and actomyosin-dependent mechanosensing trigger the recruitment of αTAT1 to FAs, and are required for rigidity-dependent microtubule acetylation.

Microtubule acetylation influences mechanotransduction at FAs

We then investigated whether microtubule acetylation may be involved in mechanosensitive cell functions. Astrocytes were sparsely plated on soft (2 kPa) and stiff (48 kPa) PAA hydrogels and stained for Yes-associated protein (YAP), an actomyosin- and RhoGTPase-dependent transcriptional activator whose nuclear translocation is mechanosensitive[27]. As is the case in several cell types[28], quantification of the nuclear-to-cytoplasmic ratio of YAP indicated that YAP nuclear localization increased when astrocytes were plated on stiff substrates compared with on soft substrates

Fig. 1 | Integrin-mediated signalling and substrate rigidity regulate microtubule acetylation. a–c, Inverted fluorescence images of WT astrocytes (**a**,**c**) and astrocytes treated with Src kin 1 or PF-562271 (**c**) and plated on PAA hydrogels. The images show acetylated tubulin and α-tubulin (**a**(i),**c**(i)) and the intensity ratio of acetylated tubulin over total tubulin (**a**(ii),**c**(ii)). The western blots show the normalized ratio of acetylated tubulin over glyceraldehyde 3-phosphate dehydrogenase (GAPDH) (**b**). $n = 77$ for 1.26 kPa, $n = 88$ for 2 kPa, $n = 67$ for 9 kPa and $n = 81$ for 48 kPa (**a**) and $n = 30$ for Ctl, $n = 43$ for Src kin1 and $n = 43$ for PF-562271 (**c**). Tub, α-tubulin; Ac-Tub, acetylated tubulin; Ctl, control. **d**,**e**, Astrocyte lysate pull-down (PD; WT cells) and immunoprecipitations (IP; cells transfected with GFP-Ctl or GFP-αTAT1) using GST or GST-αTAT1 (**d**) and GFP-Ctl or GFP-αTAT1 (**e**) resin, respectively. The western blots show talin and acetylated tubulin or GFP. **f**, Images of GFP-αTAT1 and mCherry-vinculin astrocytes transfected with siCtl or siTalin1. Ctl, control; siTalin1, siRNA targeting Talin1. **g**, Astrocytes on 48 kPa PAA gels showing acetylated tubulin and α-tubulin (i) and the ratio of the intensities of acetylated tubulin over total tubulin intensity (ii). $n = 51$ for siCtl and $n = 56$ for siTalin1. **h**, Pull-down (Ctl or Y-27632-treated cells) using GST or GST-αTAT1 resin: the western blots show talin and Ponceau staining (i) and normalized talin levels in cells treated with dimethylsulfoxide (DMSO; Ctl) or Y-27632 (ii). **i**, Images showing GFP-αTAT1- and mCherry-vinculin-expressing astrocytes treated with DMSO (Ctl) or Y-27632. **j**,**k**, Migrating astrocytes treated with DMSO (Ctl) or ROCK inhibitor Y-27632 for 2 h: western blots showing the levels of acetylated tubulin and GAPDH in the Ctl- and Y-27632-treated cells (**j**) and inverted fluorescence images of the astrocytes show acetylated tubulin and α-tubulin (**k**(i)) and ratio of acetylated tubulin intensity over total tubulin intensity (**k**(ii)). $n = 98$ for Ctl and $n = 79$ for Y-27632-treated cells. Scale bars in **a**,**c**,**g**, 10 μm; scale bars in **f**,**k**,**i**, 20 μm. Number of independent experiments = 4 (**a**,**h**), 5 (**b**,**i**), 2 (**c**), 3 (**d**–**g**,**j**,**k**). In the box-and-whisker plots, the box extends from the 25th to 75th percentile, the whiskers show minimum and maximum values, and the line within the box represents the median. Statistical tests: one-way analysis of variance (ANOVA) followed by Tukey's multiple comparison's test (**a**,**b**,**g**), paired *t*-test (**h**) and unpaired Student's *t*-test (two-tailed; **k**).

(Fig. 2a,b). In αTAT1-depleted astrocytes, the nuclear recruitment of YAP in cells plated on 48 kPa substrates was strongly inhibited, and YAP localization was similar in cells plated on soft and rigid substrates (Fig. 2a). Conversely, increasing microtubule acetylation by Tubacin treatment led to a strong nuclear recruitment of YAP in cells plated on 2 kPa substrates, recapitulating a phenotype of cells on stiff substrates (Fig. 2b). To determine whether the effects of microtubule acetylation on YAP were specific to astrocytes, we performed similar experiments on HUVECs. HUVECs exhibit a low level of acetylated tubulin, even when plated on stiff substrates

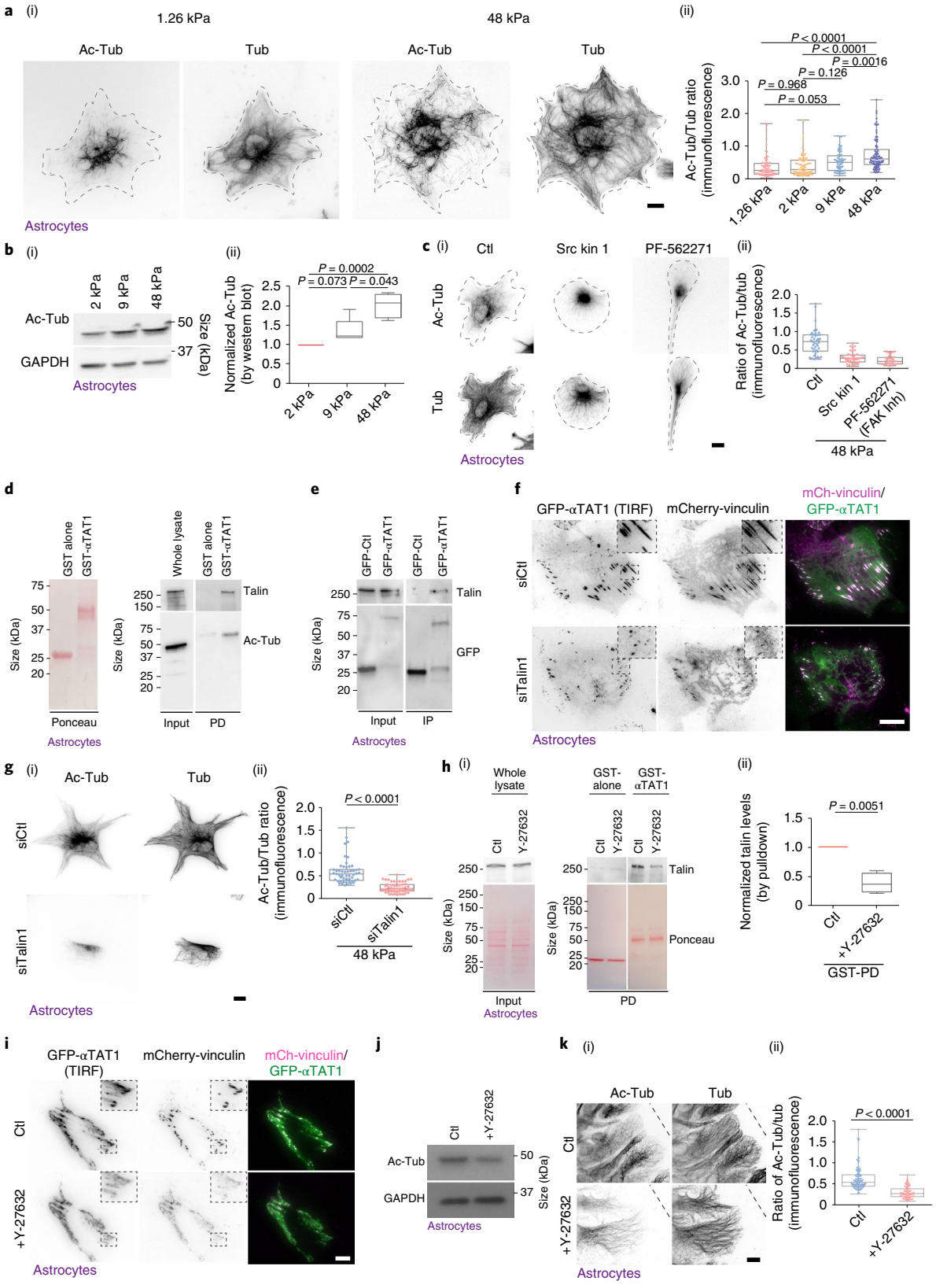

(Extended Data Fig. 3b,c). Hence, to test the effects of microtubule acetylation on YAP translocation in HUVECs, cells were treated with Tubacin to increase microtubule acetylation (Extended Data Fig. 3c). Similar to astrocytes, increasing microtubule acetylation in HUVECs plated on 2 kPa substrates resulted in an increased nuclear recruitment of YAP, mimicking the phenotype of cells plated on stiff substrates (Fig. 2c). Altogether, this demonstrates that the manipulation of microtubule acetylation tunes YAP mechanosensitive nuclear–cytoplasmic shuttling (a summary cartoon is shown in Fig. 2g).

FAs are crucial mechanosensitive structures that sense and adapt to the matrix rigidity[29]. Thus, we investigated the effects of substrate rigidity on FAs in astrocytes plated on PAA hydrogels of different rigidities, namely 1.26, 2, 9 and 48 kPa (Fig. 2d), by immunostaining the FA-associated protein paxillin[4,30]. Quantification of the density of FAs (Extended Data Fig. 3d) indicated that astrocytes plated on soft substrates display FAs throughout the cell surface, whereas FAs are predominantly found at the periphery of cells adhering to stiffer substrates (Fig. 2d). Thus, changes in substrate rigidity alter FA distribution in astrocytes, allowing us to assess the impact of microtubule acetylation in this phenomenon. Following αTAT1 depletion, FAs were distributed throughout the cell surface independently of the rigidity of the substrate, that is, αTAT1-depleted cells on stiff substrates showed a distribution of FAs similar to that of the control/siαTAT1 cells plated on soft substrates (Fig. 2e and Extended Data Fig. 3e–h). To confirm that the changes in FA distribution act through tubulin acetylation, we treated cells plated on different rigidities with Tubacin. Tubacin had no effect on FA distribution in cells plated on 48 kPa substrates (Fig. 2f and Extended Data Fig. 3e,f). In contrast, Tubacin treatment of cells plated on 1.26 kPa substrates mimicked the phenotype (FAs at the cell periphery) observed in the control/Tubacin-treated cells plated on stiff matrices (Fig. 2f and Extended Data Fig. 3e,f). Because cell spreading on different substrate rigidities can affect the distribution of FAs, we plated αTAT1-depleted cells on micropatterned hydrogels to observe FAs in cells of similar spread area. In line with our prior results, cells on soft substrates or αTAT1-depleted cells on stiffer substrates displayed FAs throughout the cell spreading area (Extended Data Fig. 3i). Together with previous findings that microtubule acetylation controls FA dynamics through the delivery of membrane vesicles at FAs[13,31], these results show that the rigidity-dependent microtubule acetylation controls the mechanosensitive distribution of FAs (Fig. 2g).

Microtubule acetylation controls cytoskeletal organization at FAs

Next, we investigated the impact of αTAT1 depletion on the FA-associated cytoskeleton. In migrating astrocytes, the actin network comprises longitudinal stress fibres connected to FAs at the front of the leader cells as well as interjunctional transverse arcs connecting neighbouring cells at adherens junctions (Fig. 3a and Extended Data Fig. 4a)[26,32]. In αTAT1-depleted cells, the transverse arcs of actin were dramatically reduced and the longitudinal fibres did not extend to the front of the migrating cells (Fig. 3a and Extended Data Fig. 4a). Associated with these longitudinal fibres, FAs were located further back within the protrusion rather than at the front of the leader cells (Fig. 3a and Extended Data Fig. 4a)[13]. Myosin light chain phosphorylation (pMLC) is predominantly seen at the leading edge of migrating control cells; however, in αTAT1-depleted cells, pMLC was barely visible at the leading edge of the cells and was only associated with the remaining actin fibres at the cell centre, similar to myosin IIA distribution (Fig. 3a,b and Extended Data Fig. 4a). Moreover, intermediate filaments (visualized using vimentin), which play a major role in regulating FAs and the collective migration of astrocytes[32] and normally extend from the perinuclear region to the cell periphery close to FAs[32,33], were absent from the front of the αTAT1-depleted cells and frequently appeared fragmented (Fig. 3c). We then looked closely at the effect of αTAT1 on the cytoskeletal organization at FAs by using platinum replica electron microscopy (PREM) on unroofed migrating astrocytes located at the wound edge. Similar to light microscopy, PREM images showed that FAs connected to actin bundles were distributed further within the protrusion in the case of siαTAT1 cells as compared with a highly organized and parallel set of FAs at the leading edge of control cells (Fig. 3d). The high magnification views of the FAs in the control cells show microtubules along actin cables reaching the FAs (marked with white arrows in Fig. 3d(i)1). Intermediate filaments could also be clearly seen, intertwined with the actin filaments at FAs (marked with yellow arrowheads in Fig. 3d(i)1,2). In siαTAT1 cells, the actin bundles near FAs were strikingly thinner than those in the controls (Fig. 3d). We consistently observed a lack of microtubules and intermediate filaments associated with FAs in αTAT1-depleted cells (Fig. 3d). All these results strongly support a role for αTAT1 in the cytoskeletal organization at FAs in astrocytes. We then explored the effects of microtubule acetylation on the cytoskeletal organization by treating HUVECs and astrocytes plated on soft substrates with Tubacin to increase microtubule acetylation. In the Tubacin-treated cells, we observed markedly larger actin cables, increased myosin IIA filaments, together with larger and more peripheral FAs (Fig. 3e and Extended Data Fig. 3b), reminiscent of the phenotype observed in astrocyte plates on stiff substrates (Fig. 3f), confirming that microtubule acetylation regulates actomyosin organization.

Microtubule acetylation increases actomyosin contractility via GEF-H1 and Rho

One major impact of mechanosensing is the adaptation of traction forces to the rigidity of the substrate[34]. We thus investigated whether microtubule acetylation might affect traction forces by plating

Fig. 2 | Microtubule acetylation tunes cell mechanosensitivity. a–c, Inverted fluorescence images of astrocytes transfected with siCtl or siαTAT1-2 (**a**) or treated with niltubacin or tubacin (**b**) and HUVECs treated with Niltubacin or Tubacin (**c**) plated on PAA gels of different rigidities stained for YAP to mark the cell boundary (marked by dotted lines; i) and the ratios of the YAP intensity in the nucleus and cytoplasm (ii). For **a**, $n=49$ for 2 kPa siCtl, $n=44$ for 2 kPa siαTAT1-2, $n=68$ for 48 kPa siCtl and $n=74$ for 48 kPa siαTAT1-2; for **b**, $n=49$ for 2 kPa Niltubacin, $n=53$ for 2 kPa Tubacin, $n=51$ for 48 kPa Niltubacin and $n=51$ for 48 kPa Tubacin; for **c**, $n=26$ for 2 kPa Niltubacin, $n=25$ for 2 kPa Tubacin, $n=32$ for 48 kPa Niltubacin and $n=26$ for 48 kPa Tubacin. **d**, WT astrocytes plated on PAA gels of different rigidities stained for α-tubulin and talin (i) and FA density (number of FAs per μm^2, denoted $N\,\mu m^{-2}$) in different regions of the cells. DAPI, 4′,6-diamidino-2-phenylindole, a DNA stain. (ii). The images shown in (i) correspond to the same cells depicted in Fig. 1a. $n=40$ for 1.26 kPa, $n=51$ for 2 kPa, $n=94$ for 9 kPa and $n=77$ for 48 kPa. **e**,**f**, Inverted fluorescence images of astrocytes transfected with siCtl or siαTAT1-2 (**e**) or treated with Niltubacin or Tubacin (**f**) plated on PAA gels of different substrate rigidity and stained for paxillin (i) and FA density in the central region (16 µm–cell centre) of the cells depicted in **e** and **f** (ii). For **e**, $n=60$ for 1.26 kPa siCtl, $n=36$ for 1.26 kPa siαTAT1-2, $n=54$ for 48 kPa siCtl and $n=47$ for 48 kPa siαTAT1-2; for **f**, $n=59$ for 1.26 kPa Niltubacin, $n=55$ for 1.26 kPa Tubacin, $n=46$ for 48 kPa Niltubacin and $n=37$ for 48 kPa Tubacin. **g**, Schematic (summarizing the findings in **a**–**f**) showing the distribution of FAs upon manipulation by microtubule acetylation. Scale bars in **a**–**f**, 10 µm. Number of independent experiments = 3 (for **a**,**b**,**d**–**f**), 2 (**c**). In the box-and-whisker plots, the box extends from the 25th to 75th percentile, the whiskers show minimum and maximum values, and the line within the box represents the median. Statistical tests: one-way ANOVA followed by Tukey's multiple comparison's test (**a**,**b**,**e**,**f**), and two-way ANOVA followed by Tukey's multiple comparison's test (**d**).

control or αTAT1-depleted astrocytes onto crossbow-shaped micropatterned hydrogels. Through traction force microscopy (TFM) experiments, we observed that αTAT1 depletion resulted in lower traction force production on 40 kPa substrates (Fig. 4a,b). In contrast, overexpression of GFP-αTAT1 increased the traction energies and forces, and also rescued the effect observed on αTAT1 knockdown (siαTAT1 + GFP-αTAT1; Fig. 4a,b) when astrocytes were plated on 40 kPa. In addition, Tubacin-treated astrocytes on

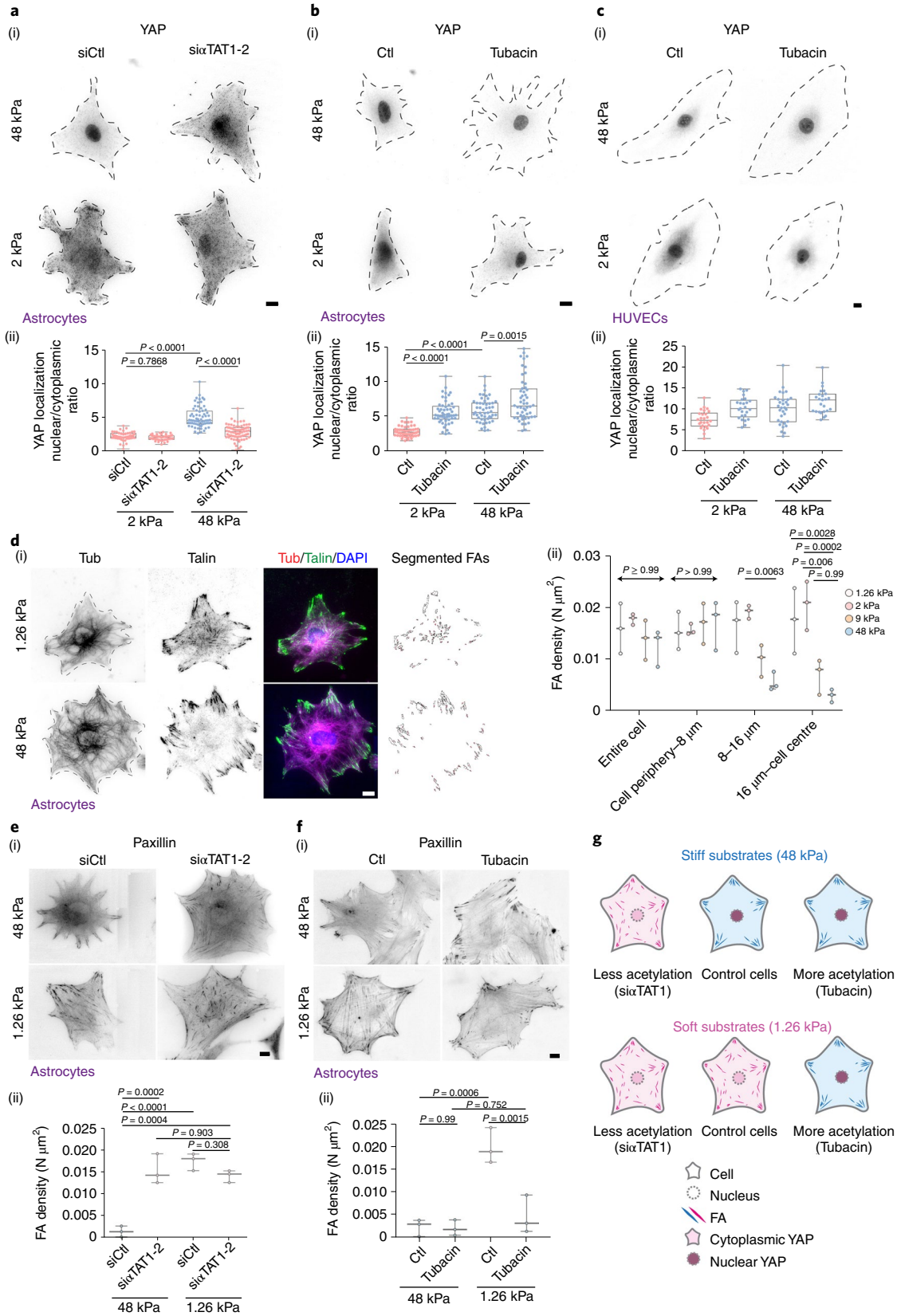

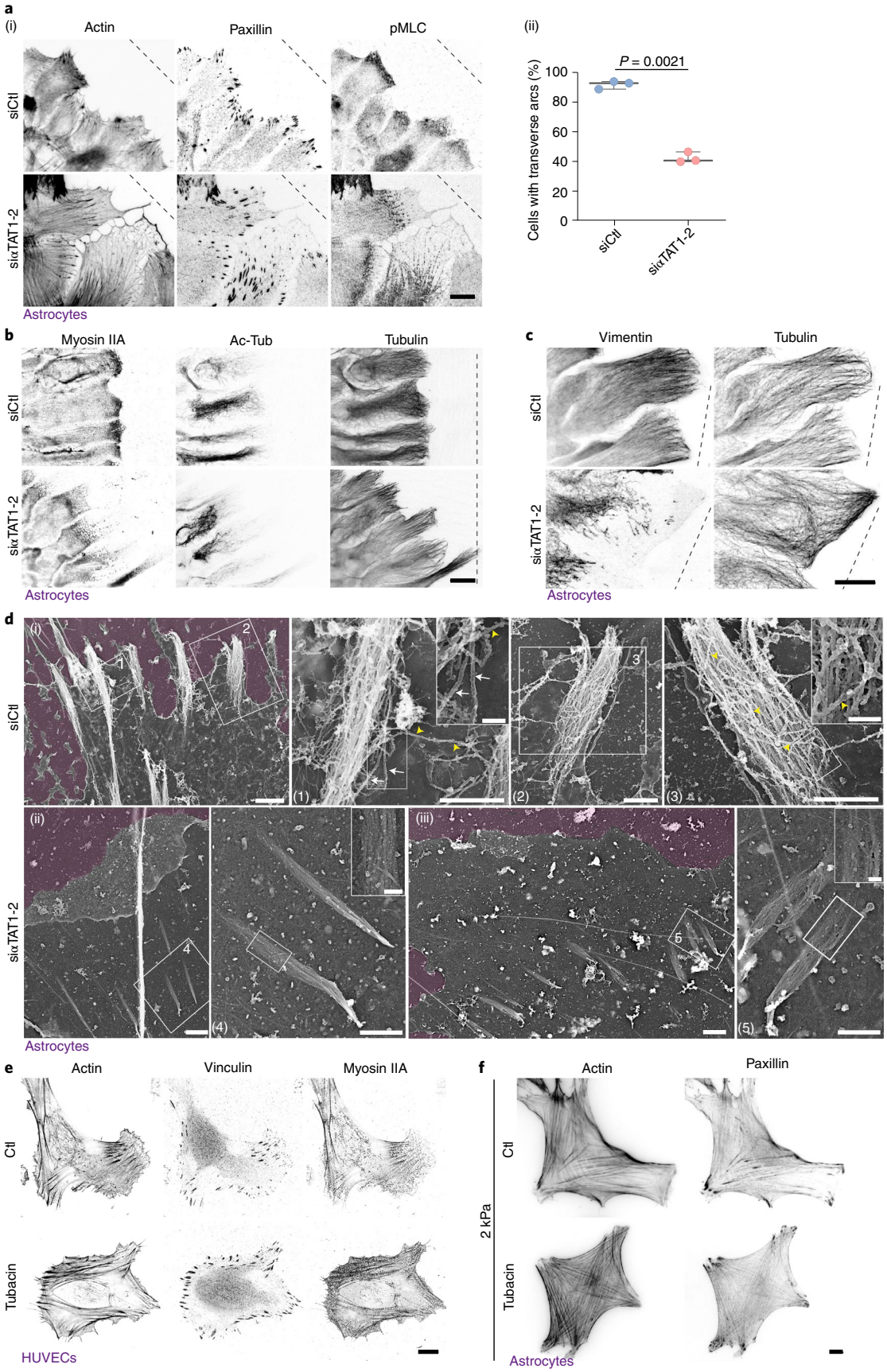

soft 2 kPa hydrogels showed increased traction energies and forces, comparable to the control astrocytes plated on 40 kPa (Fig. 4c). We also studied the effects of microtubule acetylation on traction forces in Tubacin-treated HUVECs plated on soft 2 kPa substrates. Similar to astrocytes, increased microtubule acetylation using Tubacin resulted in higher traction energies and forces in HUVECs

Fig. 3 | Microtubule acetylation reorganizes the actomyosin and intermediate filament networks. a–c, Inverted fluorescence images of astrocytes transfected with siCtl or siαTAT1 and stained for actin, pMLC and paxillin (**a**(i)), myosin IIA, acetylated tubulin and α-tubulin (**b**), and vimentin and α-tubulin (**c**), and the percentage of cells with interjunctional transverse arcs (**a**(ii)). Dashed lines indicate the position of the wound. Scale bars in **a–c**, 20 μm. $n=199$ for siCtl and $n=159$ for siαTAT1-2. **d**, Ultrastructural organization of the FA-associated cytoskeleton in siCtl and siαTAT1-2 depleted cells: platinum replica electron microscopy (PREM) survey views of the cytoplasmic surface of the leading edge in siCtl unroofed cells (i) and αTAT1-depleted cells (ii,iii). The boxed regions correspond to FAs. The extracellular space is pseudo-colored in purple. High-magnification views of the boxed images in (i), (ii) and (iii) are shown, labelled (1)–(3), (4) and (5), respectively. In the images in (1) and (3), the white arrows indicate microtubules and the yellow arrowheads denote intermediate filaments; image (3) is a magnification of image (2). Scale bars in (i), (ii) and (iii), 2 μm; scale bars in (1), (2) and (3), 1 μm; scale bars in insets of (1), (3), (4) and (5), 200 nm. **e**, HUVECs treated with DMSO or Tubacin, stained for actin, vinculin and myosin IIA. **f**, Astrocytes plated on 2 kPa PAA gels treated with Niltubacin or Tubacin, stained for actin and paxillin. Scale bars in **e**,**f**, 10 μm. In the box-and-whisker plot, the box extends from the 25th to 75th percentile, the whiskers show minimum and maximum values, and the line within the box represents the median. Number of independent experiments = 3 (**a–c**). Statistical tests: paired Student's *t*-test (two-tailed; **a**).

(Fig. 4d). Thus, the level of microtubule acetylation dictates the traction forces exerted on the substrate through FAs. This further illustrates the essential role of the mechanosensitive regulation of microtubules in force transmission.

The crucial role of microtubule acetylation in controlling cytoskeletal organization and traction forces led us to further investigate the molecular mechanisms involved in this process. We focused on RhoA, a small G protein of the Rho family, well known for promoting stress fibre formation and actomyosin contractility through its effector ROCK and pMLC. Pull-down of GTP-bound active RhoA using GST-Rhotekin beads showed that αTAT1 depletion reduced RhoA activity (Fig. 4e), suggesting that microtubule acetylation may promote actomyosin contractility by activating RhoA. RhoA activation is mediated by guanine nucleotide exchange factors (GEFs)[35]. Amongst these GEFs, GEF-H1 (also known as ARHGEF2) is a microtubule-bound RhoGEF that, when released from microtubules, triggers the Rho-ROCK signalling cascade and cell contractility[36,37]. It was previously suggested that substrate stiffness correlates with GEF-H1 activity and actomyosin contractility[38]. In addition, GEF-H1 was recently shown to be controlled by the interaction of microtubules with integrin-mediated adhesions[39], leading us to investigate whether integrin-mediated microtubule acetylation could affect the association of GEF-H1 with microtubules. In control astrocytes plated on rigid glass coverslips, GEF-H1 localized partially (approximately 42%) on microtubules, but also in the cytosol, a localization that corresponds to active/released GEF-H1 (Fig. 5a and Extended Data Fig. 5a)[40]. In contrast, in αTAT1-depleted cells, GEF-H1 was predominantly localized on microtubules (approximately 60%; Fig. 5a and Extended Data Fig. 5a). Tubacin treatment of αTAT1-depleted cells led to the release of GEF-H1 into the cytosol, rescuing the effect of αTAT1 depletion and confirming the role of microtubule acetylation in GEF-H1 localization (Fig. 5a and Extended Data Fig. 5a). In control HUVECs, which exhibit relatively low levels of acetylated tubulin, GEF-H1 was mostly bound to microtubules (approximately 50%; Fig. 5b). Similar to astrocytes, the treatment of HUVECs with Tubacin resulted in the release of GEF-H1 into the cytoplasm, with approximately only 38% of GEF-H1 colocalizing on microtubules (Fig. 5b). GEF-H1 association with microtubules was confirmed through GFP immunoprecipitation experiments using HEK cells transfected with GFP-Ctl or GFP-GEF-H1 (Fig. 5c). Similar to nocodazole treatment, which leads to the depolymerization of microtubules, Tubacin treatment (which increases microtubule acetylation) suppressed the binding of GEF-H1 to microtubules (Fig. 5c). Altogether, these results show that microtubule acetylation promotes the release of GEF-H1 from microtubules into the cytoplasm.

We then investigated whether substrate rigidity and αTAT1 play a role in the association of GEF-H1 with microtubules. Astrocytes plated on soft 2 kPa substrates exhibited a higher microtubule-bound portion of GEF-H1 as compared with cells on stiff 48 kPa gels (Fig. 5d and Extended Data Fig. 5b). In αTAT1-depleted cells plated on stiff substrates, GEF-H1 was found predominantly bound to microtubules, mimicking the phenotype observed in cells plated on soft substrates (Fig. 5d and Extended Data Fig. 5b). These results strongly suggest that rigidity-dependent microtubule acetylation contributes to mechanotransduction by enabling RhoA activation and actomyosin contractility.

Microtubule acetylation modulates mechanosensitive cell migration by tuning mechanotransduction at FAs

The involvement of microtubule acetylation in mechanotransduction and in the mechanosensitive regulation of FAs and actomyosin contractility led us to investigate its influence on cell migration, which has often been described as a mechanosensitive cellular response[2,41]. To this end, we developed a collective migration assay on hydrogels, where microdropping a small amount of a chemical (sodium hydroxide) induced a circular wound in the cell monolayer (Fig. 6a and Supplementary Video 3). Sodium hydroxide treatment did not noticeably alter the hydrogel properties (see Methods). Wild-type (WT) astrocytes migrated significantly more slowly on 2 kPa gels than on 48 kPa gels (Fig. 6b and Supplementary Video 4), implying that astrocyte migration speed is affected by substrate rigidity. Most importantly, αTAT1 depletion abolished the increased cell migration speed observed on stiff 48 kPa gels (Fig. 6c and Supplementary Video 5), so that the migration speed of αTAT1-depleted cells plated on 48 kPa was similar to that of control and αTAT1-depleted cells on 2 kPa soft substrates. In addition, the effects of αTAT1 depletion in cells plated on 48 kPa gels is in line with our previous results on the role of αTAT1 during collective migration on glass coverslips[13]. Thus, we have demonstrated that

Fig. 4 | Microtubule acetylation promotes traction force generation and RhoA activation. a–d, Stress-field maps (i) of astrocytes on crossbow-shaped micropatterned PAA gels of different rigidities, transfected with siCtl or siαTAT1-2 (**a**) or siCtl + GFP-αTAT1 or siαTAT1-2 + GFP-αTAT1 (**b**), or treated with Niltubacin or Tubacin (**c**) or HUVECs treated with Niltubacin or tubacin (**d**), and the corresponding stored energies (ii) of the cells in the above-mentioned conditions. The energies are given in joules and lie within the range of 0 and 5×10^{-13} J. For **a**, $n=163$ for siCtl and $n=141$ for siαTAT1-2; for **b**, $n=74$ for siCtl + GFP-αTAT1 and $n=70$ for siαTAT1-2 + GFP-αTAT1; for **c**, $n=136$ for Niltubacin and $n=141$ for Tubacin; for **d**, $n=83$ for Niltubacin and $n=82$ for Tubacin. **e**, GST-Rhotekin pull-downs were performed using siCtl or siαTAT1-2-transfected astrocytes. The western blots show Ponceau red and are immunoblotted for RhoA. Scale bars in **a–d**, 10 μm. Number of independent experiments = 3 (**a–e**). In the box-and-whisker plots, the box extends from the 25th to the 75th percentile, the whiskers show the minimum and maximum values, and the line within the box represents the median. Statistical tests: one-way ANOVA followed by Tukey's multiple comparison's test (**a**,**b**) and the unpaired Student's t-test (two-tailed; **c**,**d**).

microtubule acetylation is required for the mechanosensitive regulation of astrocyte collective migration.

Discussion

Our results show that microtubules are regulated in response to substrate rigidity sensing, and in turn play a key role in mechanotransduction by participating in mechanosensitive cellular responses, including translocation of the transcriptional coactivator YAP, focal adhesion distribution, actomyosin contractility, the generation of traction forces and cell migration (Fig. 6d). Our results point to a mechanism by which talin-mediated mechanosensing downstream of integrin-mediated signalling (Fig. 6d(i)) controls the recruitment of αTAT1 to FAs (Fig. 6d(ii)) and induces microtubule acetylation (Fig. 6d(iii)). We have shown that αTAT1 interacts with talin and

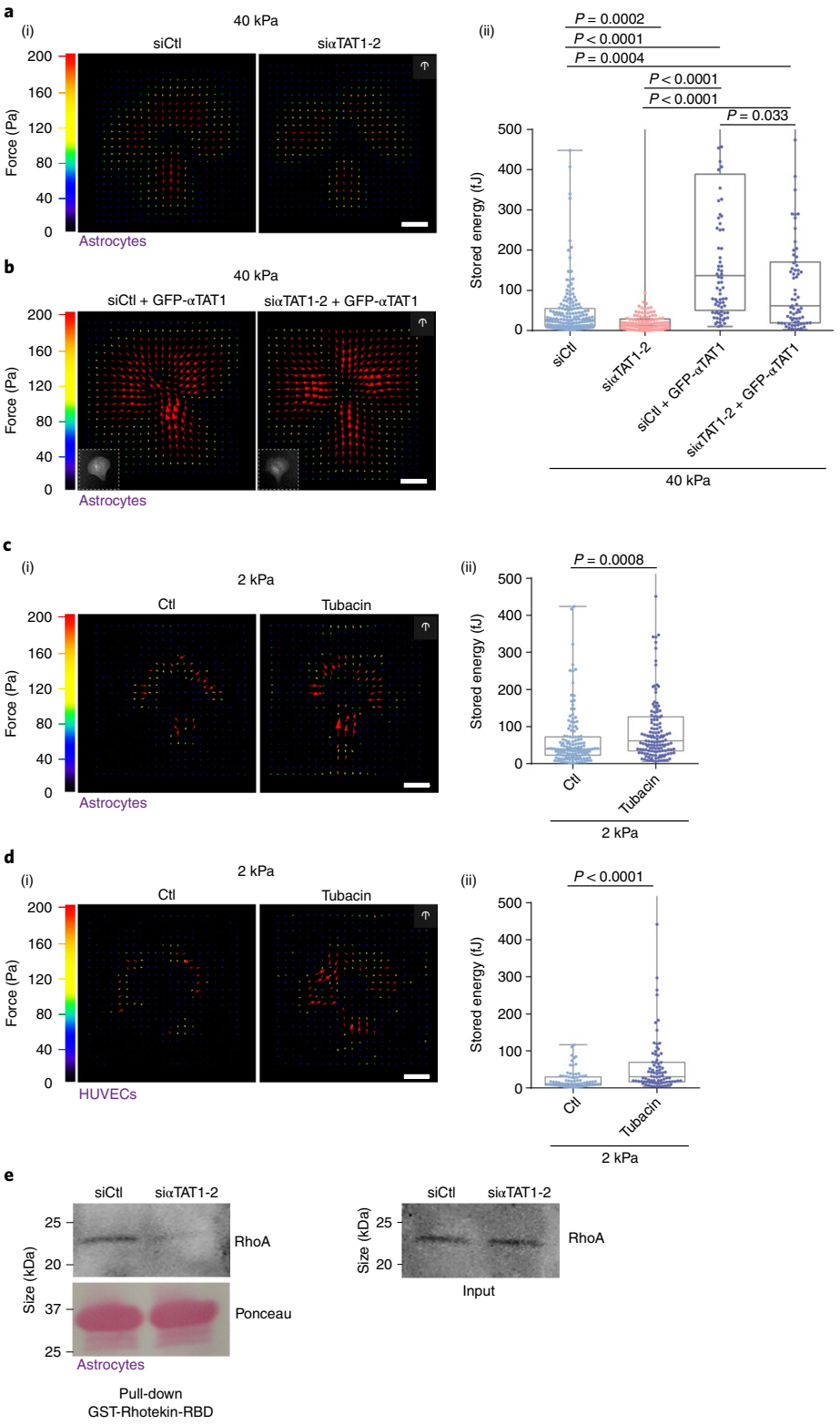

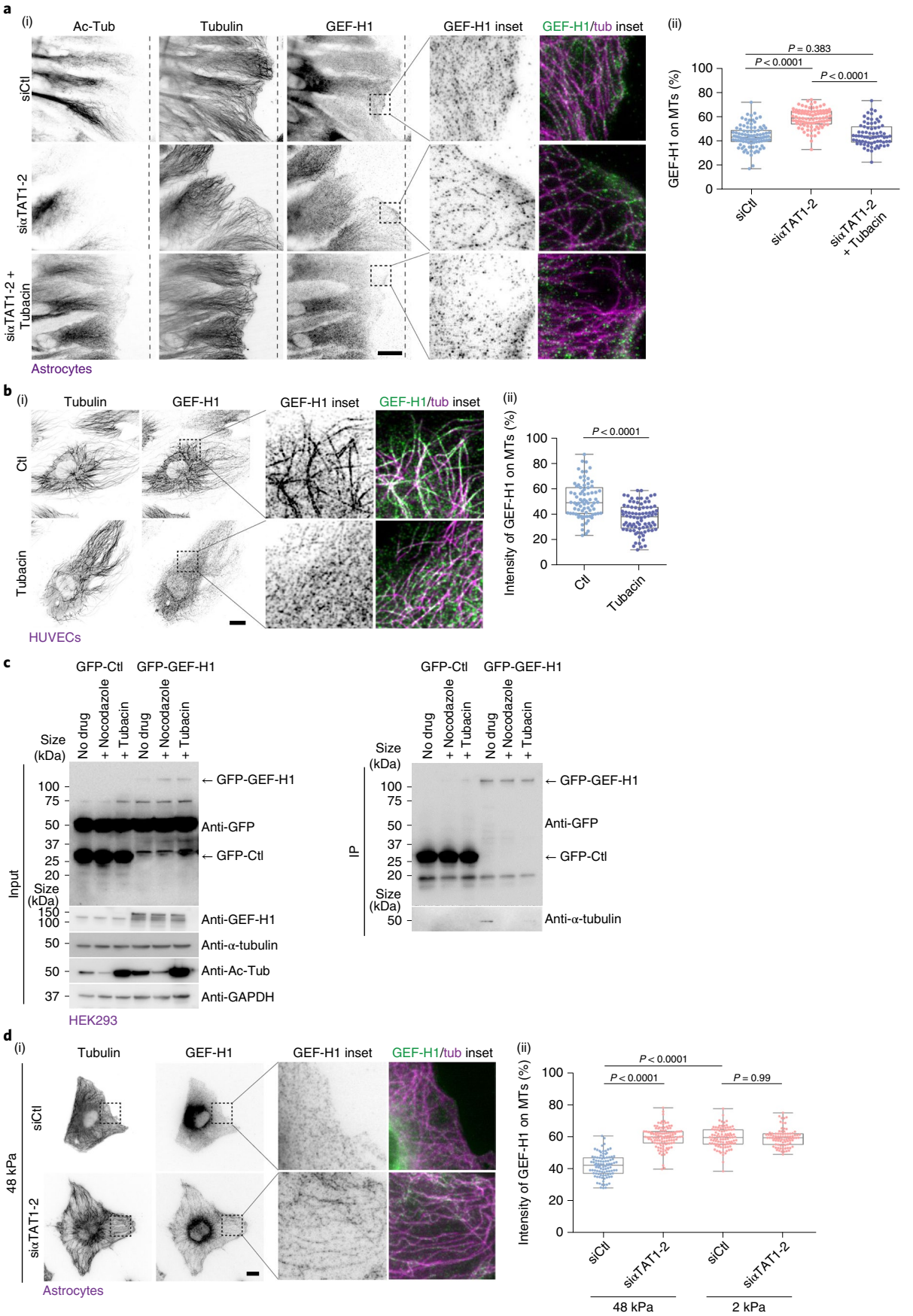
a
(i)
Ac-Tub
Tubulin
GEF-H1
GEF-H1 inset
GEF-H1/tub inset
siCtl
siαTAT1-2
siαTAT1-2 + Tubacin
Astrocytes
(ii)
P = 0.383
P < 0.0001
P < 0.0001
GEF-H1 on MTs (%)
siCtl
siαTAT1-2
siαTAT1-2 + Tubacin
b
(i)
Tubulin
GEF-H1
GEF-H1 inset
GEF-H1/tub inset
Ctl
Tubacin
HUVECs
(ii)
P < 0.0001
Intensity of GEF-H1 on MTs (%)
Ctl
Tubacin
c
GFP-Ctl
GFP-GEF-H1
No drug
+ Nocodazole
+ Tubacin
Size (kDa)
Input
← GFP-GEF-H1
Anti-GFP
← GFP-Ctl
Anti-GEF-H1
Anti-α-tubulin
Anti-Ac-Tub
Anti-GAPDH
IP
Anti-α-tubulin
HEK293
d
(i)
Tubulin
GEF-H1
GEF-H1 inset
GEF-H1/tub inset
48 kPa
siCtl
siαTAT1-2
Astrocytes
(ii)
P < 0.0001
P < 0.0001
P = 0.99
Intensity of GEF-H1 on MTs (%)
48 kPa
2 kPa

Fig. 5 | Microtubule acetylation promotes the release of GEF-H1 into the cytosol. a, Migrating astrocytes transfected with siCtl, siαTAT1-2 or siαTAT1-2 followed by treatment with Tubacin, stained for acetylated tubulin, α-tubulin and GEF-H1 (i) and the percentage of GEF-H1 colocalized with microtubules (MTs; ii). $n=99$ for siCtl, $n=89$ for siαTAT1-2 and $n=72$ for siαTAT1-2 + Tubacin. Dashed lines indicate the position of the wound. **b**, HUVECs treated with DMSO (Ctl) or Tubacin, stained for α-tubulin and GEF-H1 (i) and the percentage of GEF-H1 colocalized with microtubules (ii). $n=78$ for DMSO Ctl and $n=84$ for Tubacin. **c**, Immunoprecipitations using anti-GFP nanobodies were performed with lysates from HEK293 cells transfected with GFP-Ctl or GFP-GEF-H1 and treated with nocodazole or Tubacin. Samples were analysed by immunoblotting using α-tubulin, acetylated tubulin, GEF-H1, GAPDH and GFP antibodies. **d**, Astrocytes transfected with siCtl or siαTAT1-2, and plated on 48 kPa PAA gels, stained for GEF-H1 and α-tubulin (i) and the percentage of GEF-H1 colocalized with microtubules in cells plated on 2 and 48 kPa PAA gels (ii). $n=100$ for 48 kPa siCtl, $n=112$ for 48 kPa siαTAT1-2, $n=97$ for 2 kPa siCtl and $n=86$ for 2 kPa αTAT1-2 (1–2 regions per cell). Scale bar in **a**, 20 μm; scale bars in **b**,**d**, 10 μm. In the box-and-whisker plots, the box extends from the 25th to the 75th percentile, the whiskers show the minimum and maximum values, and the line within the box represents the median. Number of independent experiments = 3 (**a**–**d**). Statistical tests: ordinary one-way ANOVA followed by Tukey's multiple comparison's test (**a**,**d**) and unpaired Student's *t*-test followed by the Mann–Whitney test (**b**).

that, on rigid substrates, talin is required for the recruitment of αTAT1 to FAs, and for the acetylation of microtubules (Fig. 6d(ii)). Although we do not have any clear evidence of a direct interaction of talin with αTAT1, the β_1-integrin- and actomyosin-dependent association of αTAT1 with talin suggest that tension-induced changes in talin conformation may be involved in inducing αTAT1 recruitment to FAs and microtubule acetylation.

How αTAT1 enters the lumen of microtubules still remains unclear, although one can speculate that αTAT1 accesses the lumen through microtubule lattice defects or through the open ends[21]. Growing microtubule ends are often seen in close proximity to FAs at the leading edge of migrating cells[8] (Extended Data Fig. 5c). It is very likely that, like other FA-associated proteins, a large proportion of talin-associated αTAT1 rapidly exchanges with the cytosolic pool[42]. This led us to propose a model in which the increased interaction of αTAT1 with talin increases the local concentration of αTAT1 and facilitates its entry into the microtubule lumen through microtubule open ends in the vicinity of adhesions (Fig. 6d(iii) and Extended Data Fig. 5c).

We have shown that microtubule acetylation reorganizes the actomyosin network and promotes traction forces. Therefore, we propose a feedback mechanism involving crosstalk between microtubules and actin wherein actomyosin-dependent mechanosensing promotes microtubule acetylation, which, in turn, facilitates the release of GEF-H1 from microtubules into the cytosol (Fig. 6d(iv)) to increase RhoA activity (Fig. 6d(v)), cell contractility (Fig. 6d(vi)) and traction forces (Fig. 6d(vii)). It was recently shown that the uncoupling of microtubules from FAs results in a similar release of microtubule-bound GEF-H1 into the cytosol[39], which then triggers myosin IIA assembly and increased cell contractility through RhoA. Suppression of RhoA activity in the absence of αTAT1 might be due to the sequestering of GEF-H1 by non-acetylated microtubules. Whether microtubule acetylation directly or indirectly induces the release of GEF-H1 remains unclear. One can speculate that acetylation of lysine 40 changes the conformation of α-tubulin and modifies the binding site for GEF-H1, thereby inducing its release from microtubules. Alternatively, acetylation might change the mechanical properties of the microtubule lattice and affect its curvature[41,42], which would in turn facilitate the release of GEF-H1 from microtubules. It is also possible that any of the previous mechanisms affect the binding of a GEF-H1 partner, which alters the GEF-H1 conformation (for instance, through phosphorylation) and promotes its release into the cytosol. Interestingly, microtubule acetylation also affects the association of intermediate filaments with actin bundles at FAs. Because intermediate filaments have also been involved in the control of FA dynamics, actomyosin contractility as well as GEF-H1 activity[32,40], the microtubule–actin interplay described here may also involve intermediate filaments, whose role in mechanotransduction is still elusive.

In response to substrate rigidity sensing, cells adapt essential functions such as migration[43]. In the absence of αTAT1, cells plated on stiff substrates produce less traction forces and migrate more slowly (Fig. 6d(viii)). The relationship between forces and migration can be considered counterintuitive for single cell migration where traction forces appear to correlate with migration speed; and contractile forces are required for migration, but exaggerated traction forces tend to slow or even stop migration[44]. In fact, measurements of the traction forces exerted by astrocytes plated on substrates of various rigidities show that there is a rigidity optimum (around 50 kPa) at which the forces are maximal (Extended Data Fig. 5d). When looking at microtubule acetylation, actomyosin contractility or cell migration, it is clear that all of them increase up to about 48 kPa and then reach a plateau or even decrease when cells are plated on glass, indicative of a non-monotonous response. In collective cell migration, the distribution of forces within the migrating monolayer, more than the intensity itself, is crucial for the efficient control of collective cell migration. Also, collective cell migration relies on the transmission of forces between the leaders and followers. Cell–cell junctions not only transmit forces between cells, but help maintain the integrity of the monolayer[26,45], which improves collective and

Fig. 6 | Microtubule acetylation is required for mechanosensitive migration. a–**c**, Phase contrast images of WT astrocytes (**a**,**b**) or astrocytes transfected with siCtl or siαTAT1 (**c**) migrating in a chemical wound assay on PAA gels of different rigidities for 24 h (i), and migration speed of cells at the wound edge (ii). In the phase contrast images, the pink and orange dotted lines show the initial and final wound edge, respectively. $n=123$ for 2 kPa WT, $n=117$ for 9 kPa WT, $n=115$ for 48 kPa WT, $n=91$ for 2 kPa siCtl, $n=95$ for 2 kPa siαTAT1-2, $n=93$ for 48 kPa siCtl and $n=93$ for 48 kPa siαTAT1-2. Scale bar in **a**, 200 μm; scale bars in **b**,**c**, 100 μm. Number of independent experiments = 3 (**b**,**c**). Statistical tests: one-way ANOVA followed by Tukey's multiple comparison's test. In the box-and-whisker plots, the box extends from the 25th to the 75th percentile, the whiskers show the minimum and maximum values, and the line within the box represents the median. **d**, We can propose the following working models. Cells sensing a soft substrate (i) with altered integrin-signalling (ii) exhibit less microtubule acetylation (iii). This results in the binding of GEF-H1 to MTs (iv) and therefore they are unable to activate RhoA (v), which renders the cell less contractile (vi). In such conditions, cells generate low traction forces (vii) and migrate more slowly (viii). On the other hand, on stiff substrates, integrin- and talin-mediated rigidity sensing (i) promotes the tension-dependent recruitment of αTAT1 to FAs (ii) and increased microtubule acetylation (iii). How αTAT1 enters the lumen of microtubules still remains unclear, although one can speculate that the recruitment of αTAT1 at FAs increases the local cytosolic pool of the protein, which can then enter microtubules through microtubule lattice defects or through the open ends of microtubules in close proximity to FAs (Extended Data Fig. 5c). Microtubule acetylation triggers the release of GEF-H1 from MTs (iv), which activates the RhoA–ROCK–myosin IIA pathway (v) to promote actomyosin contractility (vi), traction forces (vii) and cell migration (viii).

directed cell migration. Alteration of microtubule acetylation did not induce any detachment of leader cells from followers, and did not affect directionality or persistence of migration[13]. Therefore, we propose a model in which, on stiff substrates, increased microtubule acetylation would trigger higher traction forces in leader cells, which would transmit these pulling forces to followers and increase collective migration speed. Microtubule acetylation may also affect cell migration by controlling FA dynamics. We have previously demonstrated that microtubule acetylation promotes the fusion of Rab6-dependent post-Golgi carriers at FAs and increases FA turnover[13], such that they are continuously renewed at the front of leader cells. Depletion of αTAT1 (like that of Rab6) alters the distribution of FAs in migrating cells[13]. The change in FA distribution between the cell centre and the cell periphery suggests that rigidity-induced acetylation of microtubules may promote FA turnover during cell spreading, thereby excluding them from the cell centre. We speculate

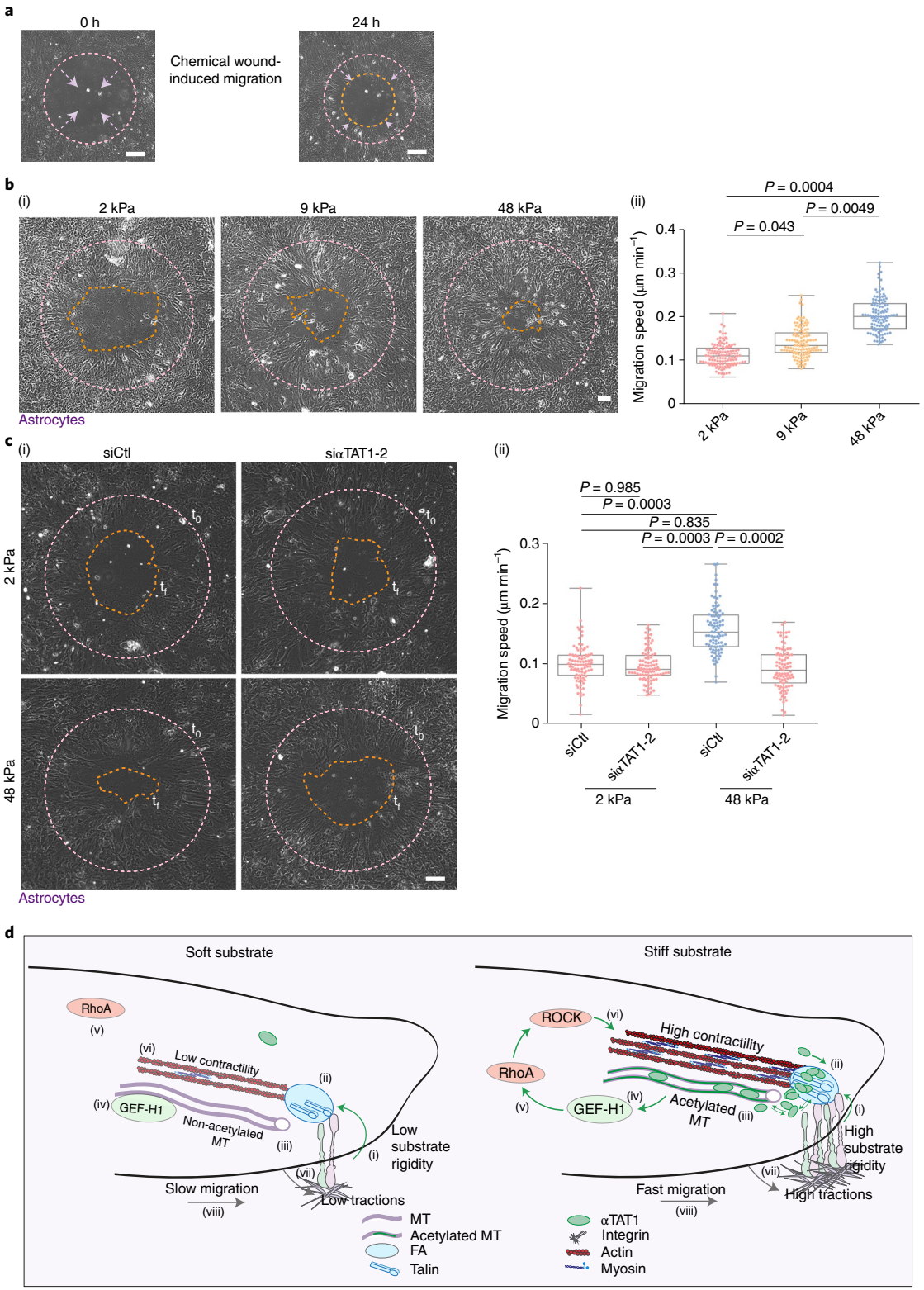

that the increase in FA turnover together with the increase in cell contractility participate in strengthening the traction forces exerted on FAs concentrated at the leader cell wound edge and improve astrocyte collective migration (Fig. 6d(viii)).

In conclusion, our results reveal crosstalk between the actin and microtubule cytoskeletal networks (Fig. 6d) whereby microtubule acetylation, downstream of rigidity-dependent integrin-mediated signalling, alters actomyosin contractility as well as focal adhesion distribution and dynamics to promote mechanosensitive migration of astrocytes, thus closing a crucial feedback loop governing mechanotransduction at FAs (Fig. 6d).

Online content

Any methods, additional references, Nature Research reporting summaries, source data, extended data, supplementary information, acknowledgements, peer review information; details of author contributions and competing interests; and statements of data and code availability are available at https://doi.org/10.1038/s41563-021-01108-x.

Received: 29 December 2019; Accepted: 20 August 2021;
Published online: 18 October 2021

References

1. Jaalouk, D. E. & Lammerding, J. Mechanotransduction gone awry. *Nat. Rev. Mol. Cell Biol.* **10**, 63–73 (2009).
2. Sun, Z., Guo, S. S. & Fässler, R. Integrin-mediated mechanotransduction. *J. Cell Biol.* **215**, 445–456 (2016).
3. Elosegui-Artola, A. et al. Rigidity sensing and adaptation through regulation of integrin types. *Nat. Mater.* **13**, 631–637 (2014).
4. Ladoux, B., Mège, R.-M. & Trepat, X. Front–rear polarization by mechanical cues: from single cells to tissues. *Trends Cell Biol.* **26**, 420–433 (2016).
5. Etienne-Manneville, S. Microtubules in cell migration. *Annu. Rev. Cell Dev. Biol.* **29**, 471–499 (2013).
6. Bouchet, B. P. & Akhmanova, A. Microtubules in 3D cell motility. *J. Cell Sci.* **130**, 39–50 (2017).
7. Martins, G. G. & Kolega, J. A role for microtubules in endothelial cell protrusion in three-dimensional matrices. *Biol. Cell* **104**, 271–286 (2012).
8. Seetharaman, S. & Etienne-Manneville, S. Microtubules at focal adhesions – a double-edged sword. *J. Cell Sci.* **132**, jcs232843 (2019).
9. Lyle, K. S., Corleto, J. A. & Wittmann, T. Microtubule dynamics regulation contributes to endothelial morphogenesis. *Bioarchitecture* **2**, 220–227 (2012).
10. Myers, K. A., Applegate, K. T., Danuser, G., Fischer, R. S. & Waterman, C. M. Distinct ECM mechanosensing pathways regulate microtubule dynamics to control endothelial cell branching morphogenesis. *J. Cell Biol.* **192**, 321–334 (2011).
11. Etienne-Manneville, S. & Hall, A. Integrin-mediated activation of Cdc42 controls cell polarity in migrating astrocytes through PKCζ. *Cell* **106**, 489–498 (2001).
12. Etienne-Manneville, S. In vitro assay of primary astrocyte migration as a tool to study Rho GTPase function in cell polarization. *Methods Enzymol.* **406**, 565–578 (2006).
13. Bance, B., Seetharaman, S., Leduc, C., Boëda, B. & Etienne-Manneville, S. Microtubule acetylation but not detyrosination promotes focal adhesion dynamics and astrocyte migration. *J. Cell Sci.* **132**, jcs.225805 (2019).
14. Coombes, C. et al. Mechanism of microtubule lumen entry for the α-tubulin acetyltransferase enzyme αTAT1. *Proc. Natl Acad. Sci. USA* **113**, E7176–E7184 (2016).
15. Valenzuela-Fernandez, A., Cabrero, J. R., Serrador, J. M. & Sánchez-Madrid, F. HDAC6: a key regulator of cytoskeleton, cell migration and cell–cell interactions. *Trends Cell Biol.* **18**, 291–297 (2008).
16. Haggarty, S. J., Koeller, K. M., Wong, J. C., Butcher, R. A. & Schreiber, S. L. Multidimensional chemical genetic analysis of diversity-oriented synthesis-derived deacetylase inhibitors using cell-based assays. *Chem. Biol.* **10**, 383–396 (2003).
17. Haggarty, S. J., Koeller, K. M., Wong, J. C., Grozinger, C. M. & Schreiber, S. L. Domain-selective small-molecule inhibitor of histone deacetylase 6 (HDAC6)-mediated tubulin deacetylation. *Proc. Natl Acad. Sci. USA* **100**, 4389–4394 (2003).
18. De Pascalis, C. & Etienne-Manneville, S. Single and collective cell migration: the mechanics of adhesions. *Mol. Biol. Cell* **28**, 1833–1846 (2017).
19. Seetharaman, S. & Etienne-Manneville, S. Integrin diversity brings specificity in mechanotransduction. *Biol. Cell* **110**, 49–64 (2018).
20. Cluzel, C. et al. The mechanisms and dynamics of αvβ3 integrin clustering in living cells. *J. Cell Biol.* **171**, 383–392 (2005).
21. Janke, C. & Montagnac, G. Causes and consequences of microtubule acetylation. *Curr. Biol.* **27**, R1287–R1292 (2017).
22. Enomoto, T. Microtubule disruption induces the formation of actin stress fibers and focal adhesions in cultured cells: possible involvement of the Rho signal cascade. *Cell Struct. Funct.* **21**, 317–326 (1996).
23. Bershadsky, A., Chausovsky, A., Becker, E., Lyubimova, A. & Geiger, B. Involvement of microtubules in the control of adhesion-dependent signal transduction. *Curr. Biol.* **6**, 1279–1289 (1996).
24. Choquet, D., Felsenfeld, D. P. & Sheetz, M. P. Extracellular matrix rigidity causes strengthening of integrin–cytoskeleton linkages. *Cell* **88**, 39–48 (1997).
25. Wolfenson, H. et al. Tropomyosin controls sarcomere-like contractions for rigidity sensing and suppressing growth on soft matrices. *Nat. Cell Biol.* **18**, 33–42 (2016).
26. Peglion, F., Llense, F. & Etienne-Manneville, S. Adherens junction treadmilling during collective migration. *Nat. Cell Biol.* **16**, 639–651 (2014).
27. Dupont, S. et al. Role of YAP/TAZ in mechanotransduction. *Nature* **474**, 179–183 (2011).
28. Panciera, T., Azzolin, L., Cordenonsi, M. & Piccolo, S. Mechanobiology of YAP and TAZ in physiology and disease. *Nat. Rev. Mol. Cell Biol.* **18**, 758–770 (2017).
29. Jansen, K. A., Atherton, P. & Ballestrem, C. Mechanotransduction at the cell-matrix interface. *Semin. Cell Dev. Biol.* **71**, 75–83 (2017).
30. Prager-Khoutorsky, M. et al. Fibroblast polarization is a matrix-rigidity-dependent process controlled by focal adhesion mechanosensing. *Nat. Cell Biol.* **13**, 1457–1465 (2011).
31. Tran, A. D.-A. et al. HDAC6 deacetylation of tubulin modulates dynamics of cellular adhesions. *J. Cell Sci.* **120**, 1469–1479 (2007).
32. De Pascalis, C. et al. Intermediate filaments control collective migration by restricting traction forces and sustaining cell–cell contacts. *J. Cell Biol.* **217**, 3031–3044 (2018).
33. Sakamoto, Y., Boëda, B. & Etienne-Manneville, S. APC binds intermediate filaments and is required for their reorganization during cell migration. *J. Cell Biol.* **200**, 249–258 (2013).
34. Schiller, H. B. et al. β_1- and α_v-class integrins cooperate to regulate myosin II during rigidity sensing of fibronectin-based microenvironments. *Nat. Cell Biol.* **15**, 625–636 (2013).
35. Lawson, C. D. & Ridley, A. J. Rho GTPase signaling complexes in cell migration and invasion. *J. Cell Biol.* **217**, 447–457 (2018).
36. Krendel, M., Zenke, F. T. & Bokoch, G. M. Nucleotide exchange factor GEF-H1 mediates cross-talk between microtubules and the actin cytoskeleton. *Nat. Cell Biol.* **4**, 294–301 (2002).
37. Ren, Y., Li, R., Zheng, Y. & Busch, H. Cloning and characterization of GEF-H1, a microtubule-associated guanine nucleotide exchange factor for Rac and Rho GTPases. *J. Biol. Chem.* **273**, 34954–34960 (1998).
38. Heck, J. N. et al. Microtubules regulate GEF-H1 in response to extracellular matrix stiffness. *Mol. Biol. Cell* **23**, 2583–2592 (2012).
39. Rafiq, N. B. M. et al. A mechano-signalling network linking microtubules, myosin IIA filaments and integrin-based adhesions. *Nat. Mater.* **18**, 638–649 (2019).
40. Jiu, Y. et al. Vimentin intermediate filaments control actin stress fiber assembly through GEF-H1 and RhoA. *J. Cell Sci.* **130**, 892–902 (2017).
41. Trepat, X. et al. Physical forces during collective cell migration. *Nat. Phys.* **5**, 426–430 (2009).
42. Legerstee, K., Geverts, B., Slotman, J. A. & Houtsmuller, A. B. Dynamics and distribution of paxillin, vinculin, zyxin and VASP depend on focal adhesion location and orientation. *Sci. Rep.* **9**, 10460 (2019).
43. Barriga, E. H., Franze, K., Charras, G. & Mayor, R. Tissue stiffening coordinates morphogenesis by triggering collective cell migration in vivo. *Nature* **554**, 523–527 (2018).
44. Leal-Egaña, A. et al. The size-speed-force relationship governs migratory cell response to tumorigenic factors. *Mol. Biol. Cell* **28**, 1612–1621 (2017).
45. Sunyer, R. et al. Collective cell durotaxis emerges from long-range intercellular force transmission. *Science* **353**, 1157–1161 (2016).

Methods

Cell culture. Primary astrocytes were obtained from E17 rat embryos[12]. These animals were used in compliance with ethical regulations and with approval from the Prefecture de Police and Direction départementale des services vétérinaires de Paris. Astrocytes were grown in 1 g l^{-1} glucose DMEM supplemented with 10% FBS (Invitrogen), 1% penicillin–streptomycin (Gibco) and 1% amphotericin B (Gibco) under 5% CO_2 at 37 °C. HUVECs were cultured in EGM-2 BulletKit medium (Lonza, catalogue no. CC-3162).

Cell nucleofection. Astrocytes were transfected with Lonza glial transfection solution and electroporated with a Nucleofector device (Lonza). The cells were then plated on appropriate supports previously coated with poly-L-ornithine (Sigma). Experiments were carried out 3 or 4 days post-transfection and comparable protein silencing was observed. siRNAs were used at 1 nmol and DNA was used at 5 µg. The siRNA sequences used were luciferase (control): 5′-UAAG GCUAUGAAGAGAUAC-3′; αTAT1 rat (siαTAT1-1): 5′-ACCGACACGUUAUU UAUGU-3′ and 5′-UUCGAAACCUGCAGGAACG-3′; αTAT1 rat (siαTAT1-2): 5′-UAAUGGAUGUACUCAUUCA-3′ and 5′-UCAUGACUAUUGUAGAUGA-3′; talin-1 rat (siTalin1): 5′-GGGACACCAUGGAGUACAGAA-3′, 5′-GACCCCCAC UUCCAGGAUAUU-3′, 5′-GCUGGAAGCUGUGGAUAACCU-3′ and 5′-GACC UCCACCCCUGAAGAUUU-3′; β_1 integrin: 5′-AUUGCCAGAUGGAGUAACA-3′.

The constructs used were GFP-αTAT1 and GST-αTAT1 (gifts from Philippe Chavrier, Institut Curie, and Guillaume Montagnac, Institut Gustave Roussy) and mCherry-vinculin. siαTAT1-1 and siαTAT1-2 were pools of two siRNAs each. For all experiments, siαTAT1-2 was used due to better knockdown efficiency, as seen in Extended Data Fig. 1a and previously characterized[13]. A few important experiments were carried out with siαTAT1-1, and the results are shown in Extended Data Figs. 1a–c, 3g,h, 4a and 5a.

Cell treatment. Cells were treated with 5–10 µM Tubacin (Sigma SMLOO65), 10 µM Niltubacin (negative control for Tubacin; Enzo Life Sciences) or DMSO (control). HUVECs were treated for 3 h, and astrocytes for 6 h. Similarly, RGD peptide (Enzo Life Sciences) or RGE control peptide (Enzo Life Sciences) was added prior to wounding. The ROCK inhibitor Y-27632 or $MnCl_2$ (1 µM) were added 6 h after wounding and 2 h before fixation. For TIRF experiments, 10 µM nocodazole or Y-27632 was added after 15 min of acquisition. For pull-downs, 10 µM nocodazole or Y-27632 was added 1 h before cell lysis.

Preparation of homogeneously coated PAA hydrogels. The protocol used to prepare PAA hydrogels was adapted from refs. [41,46,47]. Coverslips were plasma-cleaned for 3 min and silanized for 10 min using a solution of 1% (v/v) 3-(trimethoxysilyl)propyl methacrylate and 1% (v/v) acetic acid in ethanol. The coverslips were then washed twice with absolute ethanol and dried. A solution of PAA 4-(2-hydroxyethyl)-1-piperazineethanesulfonic acid (HEPES; the proportions of acrylamide and bisacrylamide in the solution define the rigidity of the hydrogel) was prepared. Then, 2.5 µl 10% ammonium persulfate (APS) and 0.25 µl tetramethylethylenediamine (TEMED) were added and the solution was mixed well. A 50 µl drop of the solution was placed on each coverslip (20 × 20 mm) and immediately an 18 × 18 mm coverslip was placed gently over the solution. The solution was allowed to polymerize for 1 h at room temperature. HEPES was added over the coverslips to detach the top glass. The polymerized gel was then activated under ultraviolet light for 5 min using Sulpho-SANPAH and washed with HEPES twice. The hydrogels were then coated with 100 µg ml^{-1} of rat tail collagen I overnight at 4 °C. The excess collagen was washed once with PBS and approximately 5×10^4 cells ml^{-1} were plated on the hydrogels.

Micropatterning. Coverslips were plasma-cleaned for 45 s and incubated with 0.1 mg ml^{-1} poly-L-lysine/polyethylene glycol (PLL-PEG) diluted in 10 mM HEPES for 30 min at room temperature. Excess PLL-PEG was allowed to slide down the coverslips by gravity, and the coverslips were then dried and stored at 4 °C overnight before printing. Micropatterns were printed on the previously prepared PLL-PEG coverslips for 3 min with specifically designed chrome masks and coated with a 50:50 (v/v) fibronectin–fibrinogen mixture (20 µg ml^{-1} each) diluted in fresh $NaHCO_3$ (pH 8.3, 100 mM) for 30 min at room temperature. The micropatterned coverslips were washed three times in $NaHCO_3$ and used immediately for transfer onto the solution of PAA hydrogel prepared in water. Plated cells (approximately 6×10^4 cells ml^{-1}) were allowed to adhere for 16 h before imaging/fixation. The crossbow patterns had an area of ~2,500 µm^2.

Traction force experiments on micropatterned substrates. After printing and coating the micropatterned coverslips, gel mixtures were prepared as follows: 40.4 kPa: 100 µl 40% acrylamide, 120 µl 2% bisacrylamide and 280 µl water (to give a final concentration of 8% acrylamide and 0.48% bisacrylamide in water); 2.61 kPa: 50 µl 40% acrylamide, 25 µl 2% bisacrylamide and 425 µl water (for a final concentration of 8% acrylamide and 0.048% bisacrylamide in water). Next, 5 µl fluorescent microbeads (FluoSpheres, Molecular Probes) were incubated with 0.1 mg ml^{-1} PLL-PEG on a rotator for 1 h at 4 °C prior to mixing with the gel mixture. The PLL-PEG-coated beads were washed and centrifuged three times at 1,000 r.p.m. for 10 min with 10 mM HEPES. These beads were then mixed with 165 µl of the gel mixture. After adding 1 µl APS and 1 µl TEMED, the solution was added as a 25 µl drop onto a silanized 20 × 20 mm coverslip. The protein-coated micropatterned coverslip was then gently placed on top of the gel mixture. The solution was allowed to polymerize for 25 min at room temperature. After detaching the micropatterned glass from the polymerized gel, 6×10^4 cells ml^{-1} were plated on the gels and allowed to adhere and spread for 16 h before TFM experiments. Stacks of single micropatterned cells were acquired before and after trypsin treatment. The acquisitions were performed with a Nikon Eclipse Ti-E epifluorescence inverted microscope with a ×40 0.6 numerical aperture (NA) air objective equipped with a pco.edge sCMOS camera and Metamorph software. Cells were maintained under 5% CO_2 at 37 °C in normal astrocyte medium during acquisition.

Migration assays. For in vitro wound-healing assays, cells were plated on the appropriate supports (dishes, plates, coverslips or glass-bottom MatTek) and grown to confluence. The cell monolayer was scratched with a p200 pipette tip to induce migration and imaged during 8 h.

For migration on soft substrates, cells were plated on hydrogels of different rigidities in six-well glass-bottom plates (MatTek) and allowed to grow for 72 h after transfection before creating a chemical wound. NaOH (0.05 M) was gently dropped onto the cells using a microinjector. The NaOH was used to instantly kill and detach cells localized in a region of a few hundred micrometres. The NaOH was added with a microinjector to deliver a fraction of a nanolitre of NaOH (0.05 M) onto a cell monolayer, which immediately mixed with 2 ml of the culture medium present in the culture dish. The dead cells and debris were gently washed away using PBS. Fresh medium was added to the cells. The cells were then placed on the microscope for live imaging. In these conditions, the hydrogel was only very locally and briefly exposed to the chemical. As the cells migrated into this space (wounded area of the monolayer), the fibronectin coating and the surface of the hydrogel remained intact with negligible and unnoticeable changes. NaOH treatment did not affect the weight of the gel, indicative of gel swelling, it did not induce any detectable bead movements, indicative of gel contraction or expansion of the gel, nor did it affect the traction forces of cells, indicating that cells did not sense any difference in substrate rigidity. Acquisition commenced 30 min after wounding. Supplementary videos were acquired with a Zeiss Axiovert 200M or Nikon Eclipse Ti-E epifluorescence inverted microscope with cells maintained under 5% CO_2 at 37 °C. All images were acquired with a dry objective ×10 0.45 NA and an EMCCD camera/pco.edge sCMOS camera and Metamorph software. Images were acquired every 15 min for 24 h. The nuclei of leader cells were manually tracked with Fiji software (Manual Tracking plug-in).

Immunostaining. Cells were fixed with cold methanol for 3 min at −20 °C or 4% warm paraformaldehyde (PFA) or 4% PFA + 0.2% glutaraldehyde + 0.25% Triton X-100 for 10 min at 37 °C. After fixation with PFA, glutaraldehyde and Triton X-100, free aldehyde groups were quenched with a solution of 1 mg ml^{-1} sodium borohydride (Sigma-Aldrich) freshly added to cytoskeletal buffer (10 mM MES or MOPS, 150 mM NaCl, 5 mM ethylene glycol-bis(β-aminoethyl ether)-*N*,*N*,*N*′,*N*′-tetraacetic acid (EGTA), 5 mM $MgCl_2$ and 5 mM glucose, pH 6.1) for 10 min on ice. The cells were permeabilized for 5 min with 0.1% Triton X-100 in the case of PFA fixation. The coverslips were blocked for 1 h with 5% bovine serum albumin (BSA) in PBS. The same solution was used for primary and secondary antibody incubation for 1 h. The nuclei were stained for DAPI and the coverslips were mounted with Prolong Gold.

Antibody anti-acetylated tubulin (1:10,000; clone 6-11B-1, mouse monoclonal, T-6793 Sigma-Aldrich or 1:200; clone 6-11B-1, ab24610, Abcam), anti-poly-Glu tubulin (1:1,000; AbC0101, ValBiotech), anti-α-tubulin (1:1,000; MCA77G, rat, Biorad), anti-paxillin (1:500; 610051, mouse monoclonal, lot 5246880, BD and ab32084, rabbit monoclonal, clone Y133, lot GR215998-1, Abcam), anti-talin (1:1,000; T3287, mouse monoclonal, clone 8D4, lot 035M4805V; Sigma-Aldrich), anti-GEF-H1 (1:100; ab155785, Abcam), Alexa Fluor 647 phalloidin (1:2,000; 176759, lot GR278180-3, Abcam or 1:300; Thermo Fisher Scientific), anti-vimentin (1:200; V6630, mouse monoclonal, lot 10M4831, Sigma-Aldrich), anti-pMLC (1:1,000; 3675S, S19, mouse, Cell Signaling), anti-myosin IIA (1:1,000; non-muscle, M8064, rabbit polyclonal, Sigma-Aldrich), anti-vinculin (1:400; V9131, Sigma-Aldrich). Secondary antibodies were Alexa Fluor 488 donkey anti-rabbit (711-545-152), tetramethylrhodamine (TRITC) donkey anti-rabbit (711-025-152), Alexa Fluor 647 donkey anti-rabbit (711-695-152), Alexa Fluor 488 donkey anti-mouse (715-545-151), rhodamine (TRITC) donkey anti-mouse (715-025-151), Alexa Fluor 647 donkey anti-rat (711-605-152) and Alexa Fluor 488 donkey anti-rat (712-545-153); all these secondary antibodies were from Jackson ImmunoResearch. Images were acquired with a Leica DM6000 microscope equipped with a ×40 1.25 NA or ×63 1.4 NA objective and recorded on a CCD camera with Leica software.

TIRF microscopy. Images were acquired with a Nikon Eclipse Ti-E epifluorescence inverted microscope with a ×60 1.49 NA oil objective equipped with a pco.edge sCMOS camera with Metamorph software. The cells were maintained under 5% CO_2 at 37 °C in normal astrocyte medium. After acquiring a 15 min movie of GFP-αTAT1 and mCherry-vinculin, nocodazole or Y27 was added and images were acquired every 2 min for 1 h.

Transmission electron microscopy. Adherent migrating astrocytes plated on glass coverslips were disrupted by sonication as described previously[48]. The coverslips were unroofed by scanning the coverslip with rapid sonicator pulses in KHMgE buffer (70 mM KCl, 30 mM HEPES, 5 mM $MgCl_2$ and 3 mM EGTA, pH 7.2). The cells, fixed with 2% paraformaldehyde and 2% glutaraldehyde, were further treated sequentially with 0.5% OsO_4, 1% tannic acid and 1% uranyl acetate prior to graded ethanol dehydration and hexamethyldisilazane substitution (Sigma-Aldrich). The samples were dried and then rotary-shadowed with 2 nm of platinum and 5–8 nm of carbon using an ACE600 high-vacuum metal coater (Leica Microsystems). Platinum replicas were floated off the glass using 5% hydrofluoric acid, washed several times by floatation on distilled water and picked up on 200 mesh formvar/carbon-coated PREM grids. The grids were mounted in a eucentric side-entry goniometer stage of a transmission electron microscope operated at 80 kV (Philips, model CM120) and images were recorded with a Morada digital camera (Olympus). The images were processed in Adobe Photoshop to adjust brightness and contrast, and presented in inverted contrast.

Image analysis. The normalized mean intensity levels of acetylated and detyrosinated tubulin in the immunofluorescence images were calculated according to equation (1):

$$\text{Ratio of acetylated/detyrosinated tubulin level} = \frac{\text{Acetylated/detyrosinated tubulin intensity}}{\text{Total tubulin intensity}}. \quad (1)$$

The YAP nuclear/cytoplasmic ratio was calculated according to equation (2):

$$\text{YAP nuclear/cytoplasmic ratio} = \frac{\text{Intensity of YAP in the nucleus}}{\text{Intensity of YAP in the cytoplasm}}. \quad (2)$$

The FA density was calculated according to equation (3):

$$\text{FA density} = \frac{\text{Number of FAs in the region}}{\text{Area of the region}}. \quad (3)$$

Different regions of cells (entire cell, cell periphery–8 µm, 8–16 µm, 16 µm–cell centre) were analysed, as depicted in Extended Data Fig. 2d.

For migration assays, the nuclei of cells were manually tracked to determine the speed, directionality and persistence of migration. The mean velocity (v), persistance (p) and directionality (d) of cell migration were calculated according to equations (4)–(6) for a given (x, y) coordinate of leading cell nucleus:

$$v = \frac{\Sigma \vartheta}{n} \quad (4)$$

$$p = \frac{\sqrt{\left[(x_{24} - x_0)^2 + (y_{24} - y_0)^2\right]}}{\sum\sqrt{\left[(x_n - x_{n-1})^2 + (y_n - y_{n-1})^2\right]}} \quad (5)$$

$$d = \frac{|(x_0 - x_{24})|}{\sum\vartheta\sqrt{\left[(x_n - x_{n-1})^2 + (y_n - y_{n-1})^2\right]}} \quad (6)$$

where n is the number of time points acquired and ϑ is the cell velocity.

The TFM images of the micropatterns were analysed using a custom-designed macro in Fiji based on a previousl study[49]. The topmost planes of beads before and after trypsinization were selected and aligned using a normalized cross-correlation algorithm (Align Slices in the Stack plug-in). The displacement field was computed from bead movements using particle image velocimetry (PIV). The parameters for the PIV analysis comprised three interrogation windows of 128, 64 and 32 pixels with a correlation of 0.60. Traction forces were calculated from the displacement field using Fourier transform traction cytometry and a Young's modulus of 40 or 2 kPa, a regularization factor of 10^{-9} and a Poisson ratio of 0.5.

For the localization of GEF-H1 on microtubules, the percentage GEF-H1 on microtubules was calculated as shown in equation (7):

$$\text{Percentage intensity of GEF} - \text{H1 localization on MT} = \frac{\text{Intensity of GEF} - \text{H1 on microtubules}}{\text{Intensity of GEF} - \text{H1 outside microtubules}} \times 100. \quad (7)$$

Immunoprecipitations and pull-down assays. Cell lysates were prepared by scraping cells in 1× lysis buffer (10× buffer recipe: 50 mM Tris pH 7.5, Triton X-100 20%, NP40 10%, 2 M NaCl with complete protease inhibitor tablet, Roche) and centrifuged for 30 min at 13,000 r.p.m. at 4 °C to pellet the cell debris. Soluble detergent extracts were incubated with GFP-Trap agarose beads (Chromotek, GTP-20) for immunoprecipitation and with GST or GST-αTAT1 beads for affinity purification for 2 h at 4 °C before washing three times with wash buffer (50 mM Tris pH 7.5, 150 mM NaCl, 0.1% Triton X-100, 1 mM EDTA and 2.5 mM $MgCl_2$). The resin was then mixed with Laemmli buffer and used for western blot and mass spectrometry analyses. HEK293 cells were used for mass spectrometry analysis to have sufficient protein from cells expressing αTAT1.

Mass spectrometry. Proteins on beads were washed twice with 100 µl of 25 mM NH_4HCO_3, and on-bead digestion was performed with 0.2 µg trypsin/Lys-C (Promega) for 1 h in 100 µl of 25 mM NH_4HCO_3. The samples were then loaded onto a home-made C18 StageTips for desalting. Peptides were eluted using 40:60 MeCN:H_2O + 0.1% formic acid and vacuum-concentrated to dryness. Online chromatography was performed with an RSLCnano instrument (Ultimate 3000, Thermo Scientific) coupled to an Orbitrap Fusion Tribrid mass spectrometer (Thermo Scientific). Peptides were trapped on a C18 column (75 µm inner diameter × 2 cm; nanoViper Acclaim PepMapTM 100, Thermo Scientific) with buffer A (2:98 MeCN:H_2O + 0.1% formic acid) at a flow rate of 4.0 µl min^{-1} over 4 min. Separation was performed on a 50 cm × 75 µm C18 column (nanoViper Acclaim PepMapTM RSLC, 2 µm, 100 Å, Thermo Scientific) regulated to a temperature of 55 °C with a linear gradient of 5 to 25% buffer B (100% MeCN + 0.1% formic acid) at a flow rate of 300 nl min^{-1} over 100 min. Full-scan mass spectra were acquired with the Orbitrap analyser with the resolution set to 120,000 and ions from each full scan were HCD-fragmented and analysed in the linear ion trap.

For identification, the data were searched against the Homo sapiens (UP000005640) SwissProt database using Sequest[HF] through Proteome Discoverer (version 2.2). The enzyme specificity was set to trypsin and a maximum of two missed cleavage sites were allowed. Oxidized methionine, N-terminal acetylation and carbamidomethyl cysteine were set as variable modifications. The maximum allowed mass deviation was set to 10 ppm for monoisotopic precursor ions and 0.6 Da for tandem mass spectroscopy peaks. The resulting files were further processed using myProMS (v3.6, work in progress)[50]. False discovery rate (FDR) calculations were performed using Percolator and the FDR at the peptide level was set to 1% for the whole study. The label-free quantifications were performed by analysing peptide extracted ion chromatograms (XICs) computed with MassChroQ (version 2.2)[51]. XICs from proteotypic peptides shared between compared conditions (TopN matching) with no missed cleavages were used for protein quantification. Median and scale normalization were applied to the total signal to correct the XICs for each biological replicate. To estimate the significance of the change in protein abundance, a linear model (adjusted on peptides and biological replicates) was performed and P values were adjusted using a Benjamini–Hochberg FDR procedure with the control threshold set to 0.05. Upregulated proteins with at least three proteotypic peptides (fold change > 1.5 and $P < 0.05$) and the unique proteins identified only in the GFP-αTAT1 were used for gene ontology (GO) enrichment analysis using GO::TermFinder tools (https://doi.org/10.1093/bioinformatics/bth456) through myProMS.

The mass spectrometry proteomics data have been deposited with the ProteomeXchange Consortium via the PRIDE (refs. [52,53]) partner repository with the dataset identifier PXD015871.

Rho activation assay. Rho activation assays were performed using a RhoA Pull-down Activation Assay Biochem Kit (Cytoskeleton, BK036-S). In short, cells were lysed in ice-cold cell lysis buffer plus 1× protease inhibitor cocktail. The cells were then centrifuged at 10,000g at 4 °C for 10 min to pellet the cell membranes and insoluble material. Part of the supernatant was stored as input for western blot analysis. The remaining supernatant was divided equally into two parts (300–800 µg protein per tube). Next, 1/15th the volume of loading buffer was added to each tube (final concentration 15 mM). Then, 1/100th the volume of GTPγS was added to one of the tubes and used as a positive control (final concentration 0.2 mM). All tubes were incubated at room temperature for 15 min. The reaction was stopped by adding 1/10th the volume of STOP buffer to all tubes (final concentration 60 mM).

Rhotekin-RBD (50 µg) beads were resuspended and added to the tubes. The tubes were rotated at 4 °C for 1 h and centrifuged at 5,000g at 4 °C for 3 min. The beads were washed with 500 µl each of wash buffer. Finally, 10–20 µl of Laemmli sample buffer was added to each tube.

Western blot. Cells lysates were obtained with Laemmli buffer composed of 60 mM Tris-HCl pH 6.8, 10% glycerol, 2% sodium dodecyl sulfate (SDS) and 50 mM dithiothreitol (DTT) with the addition of anti-protease (cOmplete cocktail, Roche 11 873 588 001). Samples were boiled for 5 min at 95 °C before loading on PAA gels. Transfer took place at 100 V for 1 h on nitrocellulose membranes. Membranes were blotted with Tris-buffered saline, 0.1% Tween 20 detergent (TBST) and 5% milk and incubated for 1 h with the primary antibody and 1 h with horseradish peroxidase (HRP)-conjugated secondary antibody. Bands were revealed using ECL chemoluminescent substrate (Biorad).

The primary antibodies used were antibody anti-acetylated tubulin (1:10,000; clone 6-11B-1, mouse monoclonal, T-6793, Sigma-Aldrich), anti-αTAT1 (1:400; rabit, HPA046816, Atlas Antibodies), anti-poly-Glu tubulin (1:1,000; AbC0101, ValBiotech), anti-α-tubulin (1:1,000; MCA77G, rat, Biorad), anti-β_1 integrin (ab52971, Abcam), anti-talin (1:1,000; T3287, mouse monoclonal, clone 8D4, lot 035M4805V, Sigma-Aldrich), anti-GEF-H1 (1:100; ab155785, Abcam) and anti-GAPDH (MAB374, lot 2689153 Millipore). The secondary HRP antibodies

were all purchased from Jackson ImmunoResearch. The unmodified western blots of Figs. 1, 4 and 5, and Extended Data Figs. 1–3 can be found in the corresponding Source data files.

Graphs and statistics. Graphpad Prism was used to create all graphs and perform all statistical analyses.

Reporting Summary. Further information on research design is available in the Nature Research Reporting Summary linked to this article.

Data availability

The data supporting the findings of this study are available within the manuscript. The mass spectrometry proteomics data have been deposited with the ProteomeXchange Consortium via the PRIDE (refs. [52,53]) partner repository with the dataset identifier PXD015871. Source data are provided with this paper. Other raw data generated during this study are available on reasonable request.

Code availability

Codes for focal adhesion distribution and traction forces are available from the authors upon request.

References

46. Serra-Picamal, X., Conte, V., Sunyer, R., Muñoz, J. J. & Trepat, X. in *Methods in Cell Biology* (ed. Paluch, E. K.) Vol. 125, 309–330 (Elsevier, 2015).
47. Tambe, D. T. et al. Collective cell guidance by cooperative intercellular forces. *Nat. Mater.* **10**, 469–475 (2011).
48. Heuser, J. The production of 'cell cortices' for light and electron microscopy. *Traffic* **1**, 545–552 (2000).
49. Martiel, J. L. et al. Measurement of cell traction forces with ImageJ. *Methods Cell. Biol.* **125**, 269–287 (2015).
50. Poullet, P., Carpentier, S. & Barillot, E. myProMS, a web server for management and validation of mass spectrometry-based proteomic data. *Proteomics* **7**, 2553–2556 (2007).
51. Valot, B., Langella, O., Nano, E. & Zivy, M. MassChroQ: a versatile tool for mass spectrometry quantification. *Proteomics* **11**, 3572–3577 (2011).
52. Vizcaino, J. A. et al. 2016 update of the PRIDE database and its related tools. *Nucleic Acids Res.* **44**, D447–D456 (2016).
53. Perez-Riverol, Y. et al. The PRIDE database and related tools and resources in 2019: improving support for quantification data. *Nucleic Acids Res.* **47**, D442–D450 (2019).

Acknowledgements

This work was supported by the La Ligue contre le cancer (S-CR17017), the Centre National de la Recherche Scientifique and Institut Pasteur. S.S. is funded by an ITN PolarNet Marie Curie grant and the Fondation pour la Recherche Médicale (FDT201904007930) and was enrolled at the Ecole Doctorale FIRE Frontières de l'Innovation en Recherche et Éducation (Frontières du Vivant FdV – Programme Bettencourt), CRI and the Université de Paris. We thank A. Akhmanova and Y.-C. Ammon for providing the GFP-talin construct, C. Leduc for the FA distribution macro and discussions, B. Bance, F. Coumailleau and O. Destaing for discussions, N. M. Rafiq for fixation protocols and discussions, and E. van Bodegraven, F. Peglion and S. Sivaranjani for critical reading of the manuscript and discussions.

Author contributions

S.S. designed and performed the experiments, analysed and interpreted the results, and wrote the paper; B.V. assisted in the set-up and analysis of TFM experiments, and helped with data interpretation and discussions; V.R. performed immunoprecipitation and pull-down experiments; A.J.F. carried out a part of the experiments using HUVECs; C.D.P. helped with experimental techniques and discussions; B.B. optimized the GFP nanobody and IP conditions used for mass spectrometry sample preparation and helped set up the chemical wound assay; F.D. carried out the MS experimental work; D.L. supervised the MS experiments and data analysis; S.V. performed the PREM experiments; A.B. helped with data interpretation and discussions; M.T. provided ideas and assisted data interpretation and discussions; S.E.-M. supervised the project, interpreted the results and wrote the paper.

Competing interests

The authors declare no competing interests.

Additional information

Extended data is available for this paper at https://doi.org/10.1038/s41563-021-01108-x.

Supplementary information The online version contains supplementary material available at https://doi.org/10.1038/s41563-021-01108-x.

Correspondence and requests for materials should be addressed to Sandrine Etienne-Manneville.

Peer review information *Nature Materials* thanks Martin Humphries, Guillaume Montagnac and the other, anonymous, reviewer(s) for their contribution to the peer review of this work.

Reprints and permissions information is available at www.nature.com/reprints.

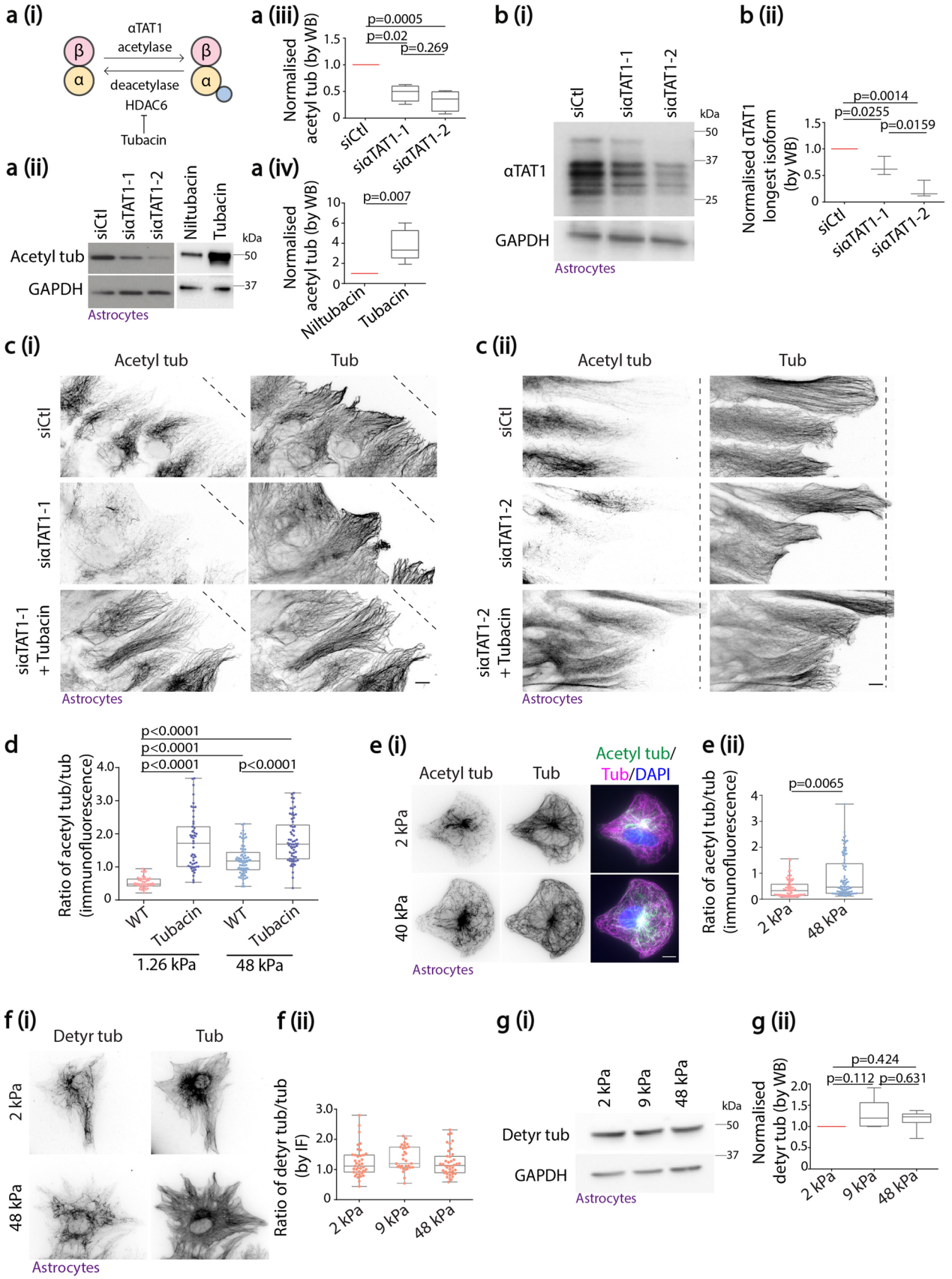

Extended Data Fig. 1 | See next page for caption.

Extended Data Fig. 1 | Substrate rigidity regulates αTAT1- dependent microtubule acetylation. a, **b**, (**a**. **i**) Schematic and (**a**. **ii**, **b**. **i**) western blots showing (**a**) acetylation and (**b**) αTAT1 levels using two distinct sets of siRNAs targeting αTAT1 (siαTAT1-1 and siαTAT1-2), and Tubacin (an inhibitor of HDAC6 (deacetylase)); (**a**. **iii**, **a**. **iv**) ratio of the acetylated tubulin or (**b**. **ii**) αTAT1 intensity over GAPDH intensity, normalized to the values observed for the respective controls. **c**, Migrating astrocytes transfected with siCtl, (**c**. **i**) siαTAT1-1 and (**c**. **ii**) siαTAT1-2, or treated with Tubacin prior to wounding, showing acetylated tubulin and α-tubulin. **d**, Astrocytes plated on PAA gels of different rigidities and treated with Tubacin; ratio of the intensities of Acetylated tubulin over total Tubulin of each cell; n = 49 for 1.26 kPa WT, 51 for 1.26 kPa Tubacin, 72 for 48 kPa WT, 66 for 48 kPa Tubacin. **e**, siCtl or WT astrocytes plated on crossbow-shaped micropatterned hydrogels of different rigidities, (**e**. **i**) showing Acetylated tubulin and α-tubulin; (**e**. **ii**) ratio of the intensities of Acetylated tubulin over total Tubulin of each cell; n = 86 for 2 kPa and 103 for 48 kPa. **f**, Astrocytes plated on PAA gels of different rigidities, (**f**. **i**) stained with Detyrosinated tubulin and α-tubulin; (**f**. **ii**) ratio of Detyrosinated tubulin over total tubulin intensities in each cell; n = 39 for 2 kPa, 31 for 9 kPa and 40 for 48 kPa. **g**, (**g**. **i**) Western blots showing the levels of Detyrosinated tubulin and GAPDH in astrocytes plated on PAA gels of different substrate rigidities; (**g**. **ii**) ratio of the intensities of Detyrosinated tubulin over GAPDH normalized to the values observed for 2 kPa. **Scale bar** (**c**, **e**, **f**): 10 μm; **Number of independent experiments** = 4 (for a - siαTAT1), 6 (for a - Tubacin, **c**, **g**), 3 (for **b**), 5 (for **e**), 2 (for **f**). In box-and-whisker plots, box extends from the 25th to 75th percentile, whiskers show minimum and maximum values, and the line within the box represents the median; **Statistical tests**: one-way ANOVA followed by Tukey's multiple comparison's test or Holm-Šídák's multiple comparisons test (a - siαTAT1, **b**, **d**, **e**, **g**) or Paired Student's t-test (for **a** - Tubacin).

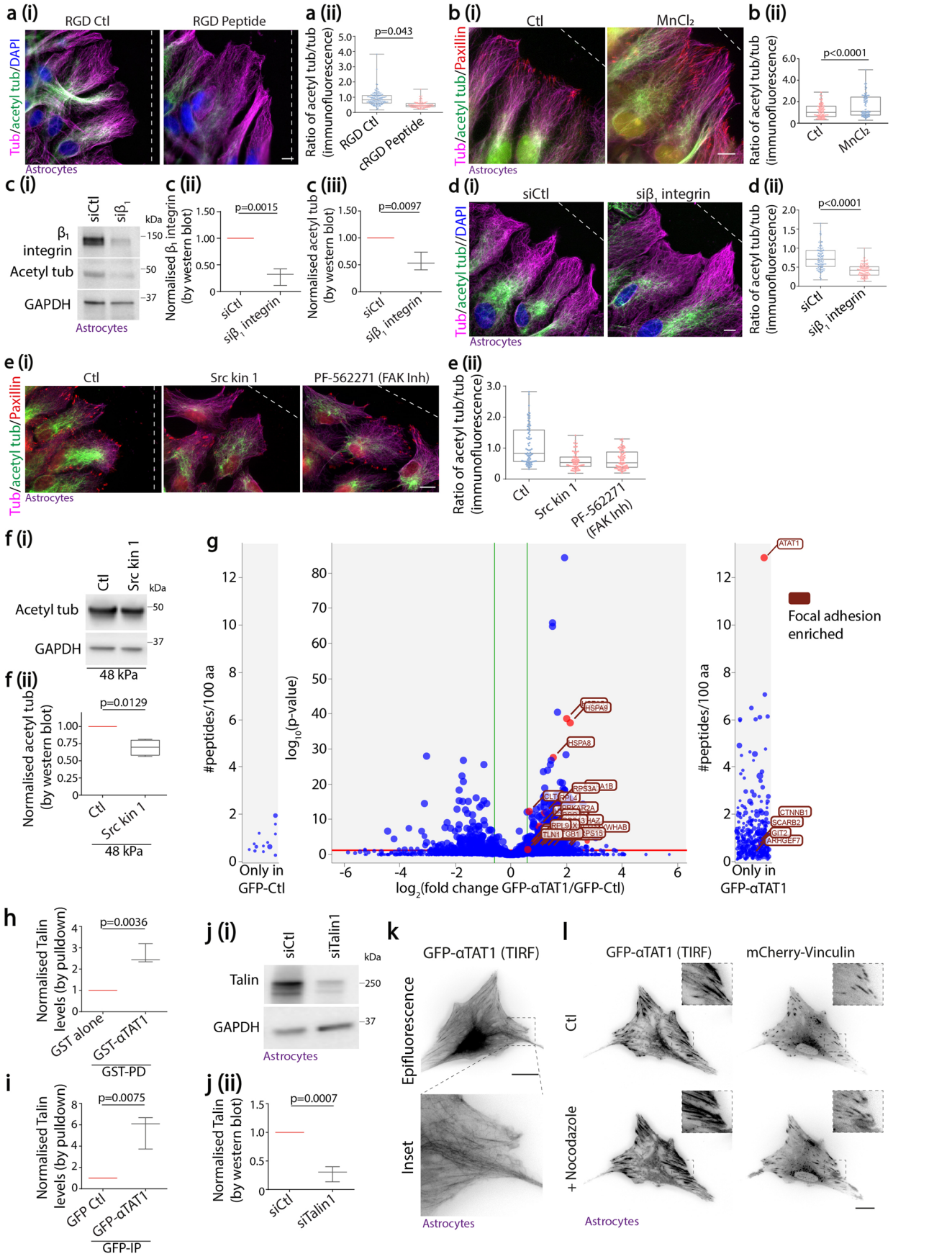

Extended Data Fig. 2 | See next page for caption.

Extended Data Fig. 2 | Integrin signaling controls microtubule acetylation and αTAT1 localization. a, **b**, Astrocytes were treated with (**a**) RGD control or RGD peptides, (**b**) solvant (Ctl) or $MnCl_2$, and (**a**. **i**, **b**. **i**) stained for acetylated tubulin, α-tubulin, paxillin or DAPI; (**a**. **ii**, **b**. **ii**) ratio of the intensities of Acetylated tubulin over total Tubulin; n = 146 for RGD control, 99 for RGD peptide, 116 for Ctl and 105 for $MnCl_2$. **c**, **d**, Astrocytes were transfected with siCtl or siβ_1 integrin; (**c**. **i**) Western blots showing levels of β_1 integrin, Acetylated tubulin and GAPDH; (**c**. **ii**, **iii**) ratio of intensities of β_1 integrin or Acetylated tubulin over GAPDH, normalized to the levels in siCtl respectively; (**d**. **i**) stained for Acetylated tubulin, α-tubulin and DAPI; (**d**. **ii**) ratio of the intensities of Acetylated tubulin over total Tubulin; n = 122 for siCtl and 117 for siβ_1 integrin. **e**, Astrocytes were treated with Ctl, Src kin 1 or PF-562271; (**e**. **i**) stained for Acetylated tubulin, α-tubulin and Paxillin; (**e**. **ii**) ratio of the intensities of Acetylated tubulin over total Tubulin intensity; n = 78 for Ctl, 70 for Src kin 1, 79 for PF-562271. **f**, Astrocytes were plated on 48 kPa gels and treated with Ctl or Src kin 1. (**f**. **i**) Western blots showing the levels of Acetylated tubulin and GAPDH; (**f**. **ii**) ratio of the intensities of Acetylated tubulin over GAPDH normalized to the Ctl. **g**, Volcano plot analysis showing fold changes (GFP-αTAT1/GFP-Ctl) of the quantified proteins with threshold of >3 peptides, minimum absolute fold change of 1.5 (green lines) and maximum adjusted p-value of 0.05 (red line). Enriched protein interactors related to GO:0005925 focal adhesion (red boxes; ratio = 1.98 and $p = 7.89 \times 10^{-5}$). External plots show proteins with peptides identified only in one sample type (left in GFP-Ctl and right in GFP-αTAT1). **h**, **i**, Normalized Talin interaction in (h) GST-pulldown and (i) GFP-immunoprecipitations. **j**, Western blots (**j**. **i**) showing the levels of Talin and GAPDH in astrocytes transfected with siCtl and siTalin; (**j**. **ii**) ratio of the intensities of Talin over GAPDH normalized to the Ctl. **k**, **l**, Astrocytes showing (**k**) GFP-αTAT1 localization by epifluorescence, on microtubules, (**l**) by TIRF, at FAs, in cells treated with or without nocodazole. **Scale bar** (**a**, **b**, **d**, **e**, **k**, **l**): 10 μm; **Number of independent experiments** = 3 (for **a**–**d**, **h**–**j**), 2 (for **e**), 4 (for **f**, **g**), 5 (for **l**). In box-and-whisker plots, the box extends from the 25th to the 75th percentile, whiskers show the minimum and maximum values, and the line within the box represents the median; **Statistical tests:** Student's t-test (for **a**–**j**).

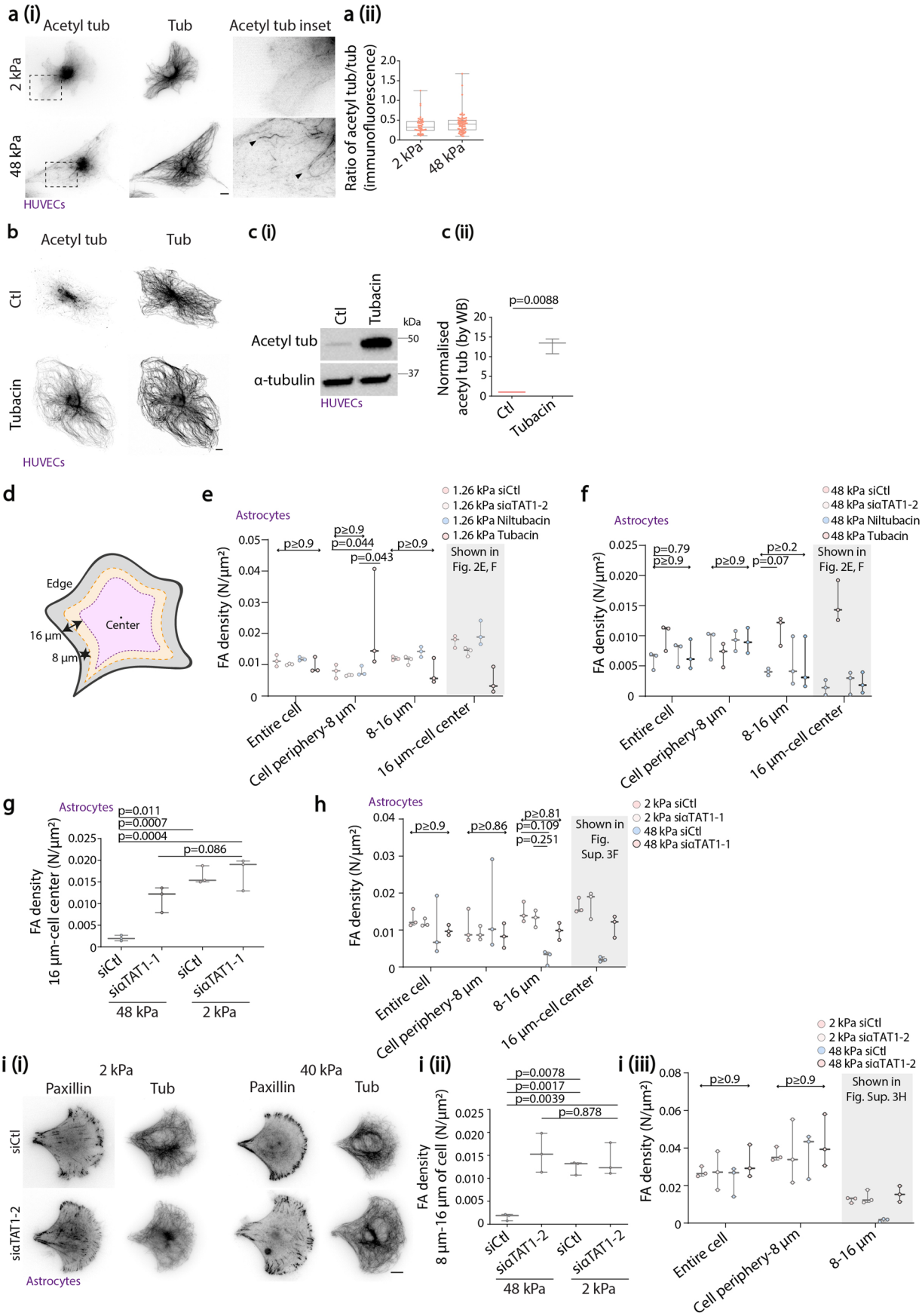

Extended Data Fig. 3 | See next page for caption.

Extended Data Fig. 3 | Microtubule acetylation controls focal adhesion distribution. a, HUVECs plated on different substrate rigidities and (**a**. **i**) stained for Acetylated tubulin (insets shown) and α-Tubulin; (**a**. **ii**) ratio of the intensities of Acetylated tubulin over total Tubulin of each cell; n = 46 for 2 kPa WT and 70 for 48 kPa. **b**, HUVECs treated with Niltubacin (Ctl) or Tubacin, and stained for Acetylated tubulin (insets shown), α-tubulin and Paxillin. **c**, Western blots showing (**c**. **i**) Acetylated and α-tubulin levels in HUVECs treated with DMSO (Ctl) and Tubacin; (**c**. **ii**) ratio of intensities of Acetylated tubulin over α-tubulin. **d**, Schematic representation of the different cell regions used to quantify FA density (Fig. 2d–f). **e**, **f**, Graphs show FA density (number of FAs/μm^2) in different regions of astrocytes transfected with siCtl or siαTAT1-2, or treated with Niltubacin or Tubacin, and plated on 1.26 kPa or 48 kPa substrates. **g**, **h**, Graphs show FA density (number of FAs/μm^2) in different regions of astrocytes transfected with siCtl or siαTAT1-1, and plated on 1.26 kPa or 48 kPa substrates. **i**. siCtl or siαTAT1-2-transfected astrocytes plated on crossbow-shaped micropatterned polyacrylamide gels of 40 kPa or 2 kPa, (**i**. **i**) stained with Paxillin and α-tubulin; (**i**. **ii**) FA density (number of FAs/μm^2) within 8-16 μm layer of the cell, or (**i**. **iii**) in different regions of astrocytes transfected with siCtl or siαTAT1-2, and plated on 2 kPa or 40 kPa substrates. **Scale bar** (**a**, **b**, **i**): 10 μm. **Number of independent experiments** = 2 (for **a**), 3 (for **b**, **e**–**i**). In box-and-whisker plots, the box extends from the 25th to the 75th percentile, the whiskers show the minimum and maximum values, and the line within the box represents the median. **Statistical tests:** Paired Student's t-test (for **c**), one-way ANOVA followed by Tukey's multiple comparisons test (for **e**–**i**).

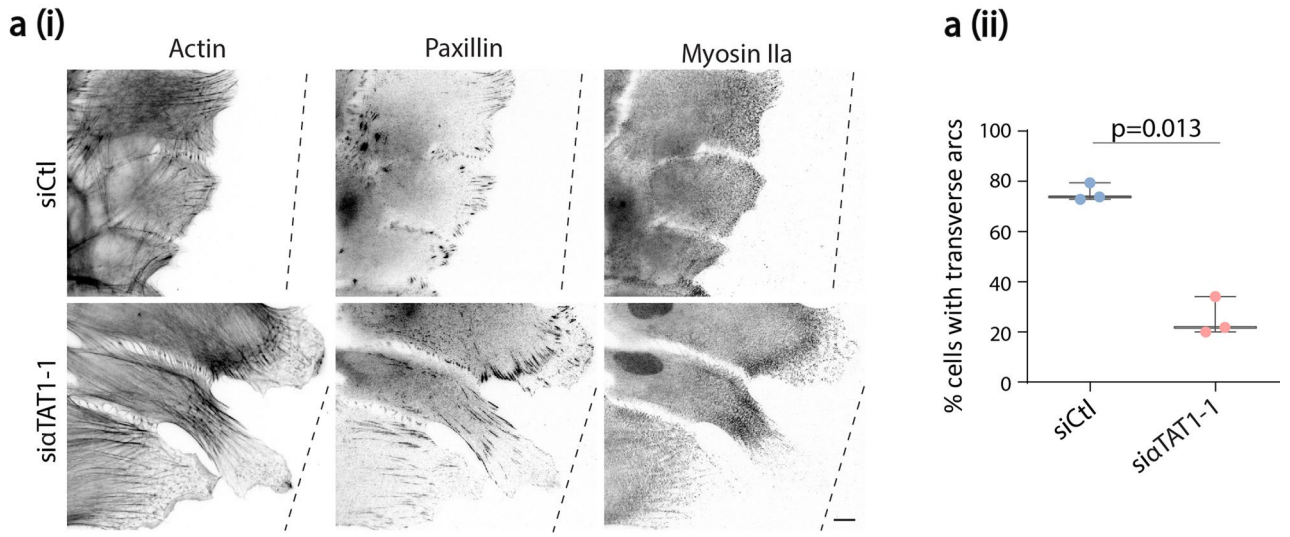

Extended Data Fig. 4 | Microtubule acetylation promotes acto-myosin contractility. a, Astrocytes transfected with siCtl or siαTAT1-1, and (**a**. **i**) stained for Actin, Paxillin and Myosin IIa; (**a**. **ii**) percentage of siCtl or siαTAT1-transfected astrocytes with transverse interjunctional actin arcs; n = 191 for siCtl and 125 for siαTAT1-1; **Scale bar**: 10 µm. **Number of independent experiments** = 3; **Statistical test:** Paired Student's t-test (two-tailed).

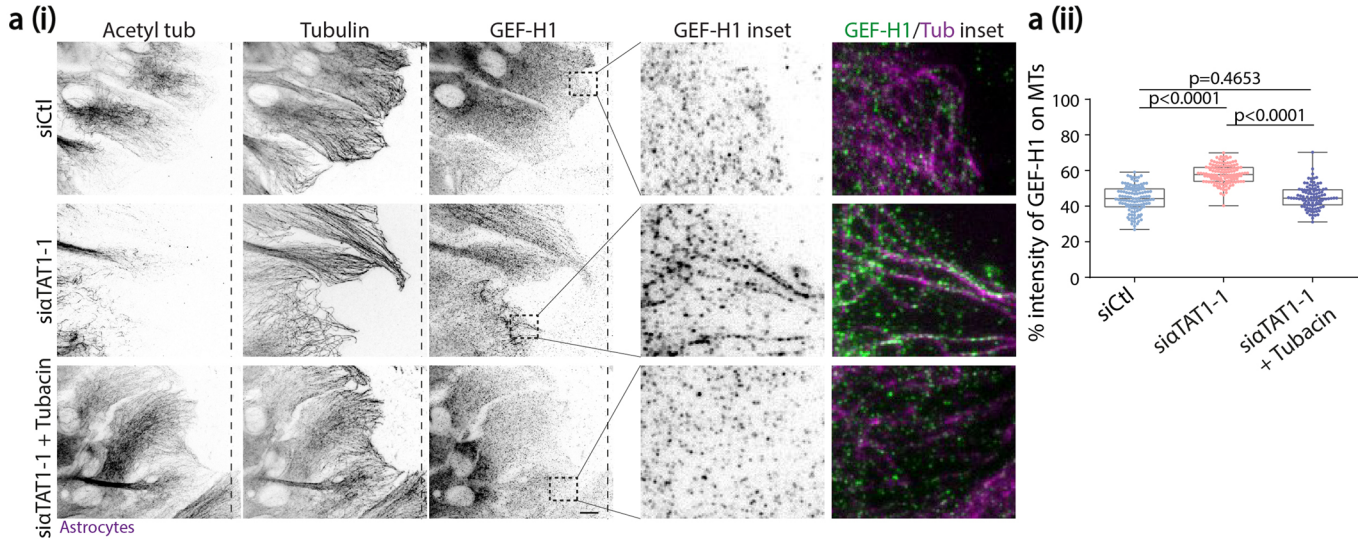

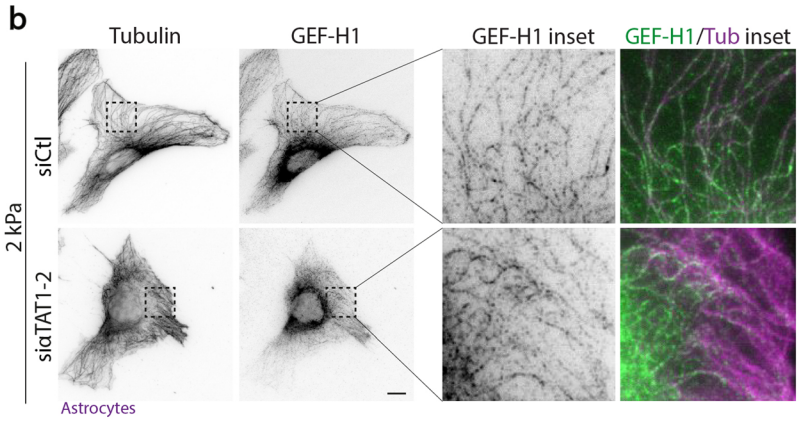

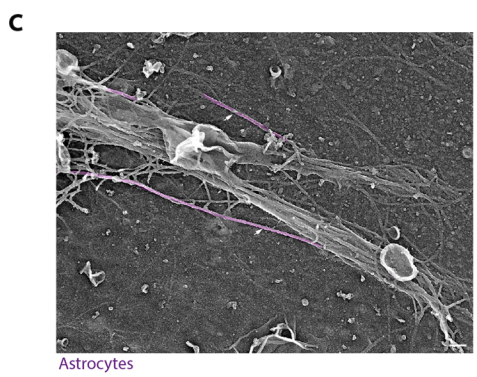

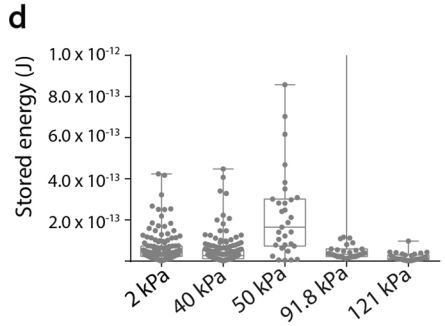

Extended Data Fig. 5 | See next page for caption.

Extended Data Fig. 5 | Microtubule acetylation controls GEF-H1 association with microtubules. a, Migrating astrocytes transfected with siCtl, siαTAT1-1 and siαTAT1-1 treated with Tubacin, (**a**. **i**) stained for Acetylated tubulin, α-tubulin and GEF-H1; (**a**. **ii**) percentage of GEF-H1 colocalized with microtubules; n = 119 for siCtl, 131 for siαTAT1-1, 103 for siαTAT1-1 + Tubacin. **b**, Astrocytes transfected with siCtl and siαTAT1-2, and plated on 2 kPa PAA gels, stained for GEF-H1 and α-tubulin. **c**, Ultrastructural organization of a focal adhesion at the leading edge of a control astrocyte. Platinum replica electron microscopy (PREM) high magnification view of a focal adhesion on the cytoplasmic surface of the leading edge in siCtl unroofed astrocytes. Microtubules are both colored in purple and indicated by white arrowheads. **d**, Traction forces in astrocytes plated on micropatterned polyacrylamide gels of different rigidities; traction forces for cells on different rigidities; Values for 2 kPa and 48 kPa are from experiments shown in Fig. 4a, b, pooled along with the values for 50 kPa, 91.8 kPa and 121 kPa; n = 136 for 2 kPa Niltubacin, 163 for 48 kPa siCtl, 31 for 50 kPa WT, 33 for 91.8 kPa WT and 30 for 121 kPa WT. In box-and-whisker plots, the box extends from the 25th to the 75th percentile, the whiskers show the minimum and maximum values, and the line within the box represents the median. **Scale bar** (**a**, **b**): 10 μm, (**c**): 200 nm; **Number of independent experiments** = 3 (for **a**, **b**, **d** - 2 kPa Niltubacin and 48 kPa siCtl), 2 (for **d** - 50 kPa, 91.8 kPa and 121 kPa). **Statistical tests:** One-way ANOVA followed by Tukey's multiple comparison's test (for **a**).

nature research

Corresponding author(s): Sandrine ETIENNE-MANNEVILLE

Last updated by author(s): Aug 4, 2021

Reporting Summary

Nature Research wishes to improve the reproducibility of the work that we publish. This form provides structure for consistency and transparency in reporting. For further information on Nature Research policies, see Authors & Referees and the Editorial Policy Checklist.

Statistics

For all statistical analyses, confirm that the following items are present in the figure legend, table legend, main text, or Methods section.

n/a	Confirmed
☐	☒ The exact sample size (*n*) for each experimental group/condition, given as a discrete number and unit of measurement
☐	☒ A statement on whether measurements were taken from distinct samples or whether the same sample was measured repeatedly
☐	☒ The statistical test(s) used AND whether they are one- or two-sided *Only common tests should be described solely by name; describe more complex techniques in the Methods section.*
☒	☐ A description of all covariates tested
☒	☐ A description of any assumptions or corrections, such as tests of normality and adjustment for multiple comparisons
☐	☒ A full description of the statistical parameters including central tendency (e.g. means) or other basic estimates (e.g. regression coefficient) AND variation (e.g. standard deviation) or associated estimates of uncertainty (e.g. confidence intervals)
☐	☒ For null hypothesis testing, the test statistic (e.g. *F*, *t*, *r*) with confidence intervals, effect sizes, degrees of freedom and *P* value noted *Give P values as exact values whenever suitable.*
☒	☐ For Bayesian analysis, information on the choice of priors and Markov chain Monte Carlo settings
☒	☐ For hierarchical and complex designs, identification of the appropriate level for tests and full reporting of outcomes
☒	☐ Estimates of effect sizes (e.g. Cohen's *d*, Pearson's *r*), indicating how they were calculated

Our web collection on statistics for biologists contains articles on many of the points above.

Software and code

Policy information about availability of computer code

Data collection	Nikon microscopes coupled with Metamorph® or Leica microscopes coupled with Leica Application Software LAS AF 2.4 (Leica Application Suite).were used for image acquisition.
Data analysis	ImageJ version 1.52n was used for all image analysis and processing. For focal adhesion density and TFM, a custom macro was used and calculations were done as described in the materials and methods. ImageJ plugin for TFM was downloaded from https://sites.google.com/site/qingzongtseng/tfm. For mass spectrometry data analysis, SequestHF through proteome discoverer (version 2.2), myProMS 45 v3.6, MassChroQ version 2.2 softwares were used. Graphpad Prism 6 was used for data representation and statistical analyses.

For manuscripts utilizing custom algorithms or software that are central to the research but not yet described in published literature, software must be made available to editors/reviewers. We strongly encourage code deposition in a community repository (e.g. GitHub). See the Nature Research guidelines for submitting code & software for further information.

Data

Policy information about availability of data

All manuscripts must include a data availability statement. This statement should provide the following information, where applicable:

- Accession codes, unique identifiers, or web links for publicly available datasets
- A list of figures that have associated raw data
- A description of any restrictions on data availability

The data supporting the findings of this study are available within the manuscript. All the raw data generated during this study are available from the corresponding author on reasonable request. The mass spectrometry data has been uploaded on the ProteomeXchange Consortium via the PRIDE partner repository with the dataset identifier PXD015871 (username: reviewer89842@ebi.ac.uk; password: EC4DSdRf (Check materials and methods on details of how to access the data).

Unmodified westernblots of figures 1, 4 and 5, as well as extended data Figure 1, 2 and 3 can be found in the corresponding source data files.

Field-specific reporting

Please select the one below that is the best fit for your research. If you are not sure, read the appropriate sections before making your selection.

☒ Life sciences ☐ Behavioural & social sciences ☐ Ecological, evolutionary & environmental sciences

For a reference copy of the document with all sections, see nature.com/documents/nr-reporting-summary-flat.pdf

Life sciences study design

All studies must disclose on these points even when the disclosure is negative.

Sample size	The sample size was limited by experimental constraints. The authors however estimated that the size was sufficiently high to represent faithfully the total population by considering the dispersion of values and their density around the most frequent value. In all cases, a minimum of three independent experiments were carried out to confirm the reproducibility of the data
Data exclusions	No data were excluded
Replication	All experiments were reproduced independently at least 3 times (unless otherwise stated), starting with primary cells produced from different animals.
Randomization	All biochemical samples were analyzed. For cell analysis, cells were randomly chosen and imaged without any bias.
Blinding	Data acquisition was performed blindly. Researchers were unblinded for data analysis. Automatic quantitative measurements by the relevant softwares and devices did not require blinding.

Reporting for specific materials, systems and methods

We require information from authors about some types of materials, experimental systems and methods used in many studies. Here, indicate whether each material, system or method listed is relevant to your study. If you are not sure if a list item applies to your research, read the appropriate section before selecting a response.

Materials & experimental systems

n/a	Involved in the study
☐	☒ Antibodies
☐	☒ Eukaryotic cell lines
☒	☐ Palaeontology
☐	☒ Animals and other organisms
☒	☐ Human research participants
☒	☐ Clinical data

Methods

n/a	Involved in the study
☒	☐ ChIP-seq
☒	☐ Flow cytometry
☒	☐ MRI-based neuroimaging

Antibodies

Antibodies used	For Immunofluorescence: Antibody anti-Acetylated Tubulin (1:10000; clone 6-11B-1, mouse monoclonal, T-6793 Sigma Aldrich or 1:200; clone 6-11B-1, ab24610, Abcam), anti-Poly-Glu Tubulin (1:1000; AbC0101, ValBiotech), anti-α-Tubulin (1:1000; MCA77G, rat, Biorad), anti-Paxillin (1:500; 610051, mouse monoclonal, lot 5246880; BD; and ab32084, rabbit monoclonal, clone Y133 and lot GR215998-1; Abcam), anti-Talin (1:1000; T3287, mouse monoclonal, clone 8D4, lot 035M4805V; Sigma-Aldrich), anti-GEF-H1 (1:100; ab155785, Abcam), Alexa fluor 647 Phalloidin (1:2000; 176759, lot GR278180-3; Abcam or 1:300; Thermo Fisher Scientific), anti-Vimentin (1:200; V6630, mouse monoclonal lot 10M4831; Sigma-Aldrich), anti-pMLC (1:1000; 3675S, S19, mouse, Cell signalling), anti-Myosin IIA (1:1000; non-muscle, M8064, rabbit polyclonal, Sigma-Aldrich), anti-Vinculin (1:400; V9131, Sigma-Aldrich). Secondary antibodies were Alexa Fluor 488 donkey anti–rabbit (711-545-152), Rhodamine (TRITC) donkey anti–rabbit (711-025-152), Alexa Fluor 647 donkey anti–rabbit (711-695-152), Alexa Fluor 488 donkey anti–mouse (715-545-151), Rhodamine (TRITC) donkey anti–mouse (715-025-151), Alexa Fluor 647 donkey anti-rat (711-605-152), and Alexa Fluor 488 donkey anti–rat (712-545-153); all from Jackson ImmunoResearch. For Western Blots : Antibody anti-Acetylated Tubulin (1:10000; clone 6-11B-1, mouse monoclonal, T-6793 Sigma Aldrich), anti-αTAT1 (1:400; HPA046816, rabbit, Atlas Antibodies), anti-Poly-Glu Tubulin (1:1000; AbC0101, ValBiotech), anti-α-Tubulin (1:1000; MCA77G, rat, Biorad), anti-β1 integrin (ab52971, Abcam), anti-Talin (1:1000; T3287, mouse monoclonal, clone 8D4, lot 035M4805V; Sigma-Aldrich), anti-GEF-H1 (1:100; ab155785, Abcam), anti-GAPDH (MAB374, lot 2689153 Millipore). Secondary HRP antibodies were all purchased from Jackson ImmunoResearch.
Validation	Anibodies were validated by the manufacturer. We verified that the antibodies showed proteins of the correct size by westernblotting. Potential anibody crossreaction, and antibody validity with rat proteins was evaluated by using rat and human cells in parallel and by testing samples obtained from cells in which the protein of interest had been depleted or overexpressed

in a tagged version.

Eukaryotic cell lines

Policy information about cell lines

Cell line source(s)	HEK293T (ATCC #CRL-11268TM
Authentication	The cell line was not authenticated after purchase
Mycoplasma contamination	Cell lines regularly tested negative for Mycoplasma contamination.
Commonly misidentified lines (See ICLAC register)	No commonly misidentified cell lines were used

Animals and other organisms

Policy information about studies involving animals; ARRIVE guidelines recommended for reporting animal research

Laboratory animals	Primary astrocytes were obtained from E17 OFA rat embryos
Wild animals	No wild animals were used in this study
Field-collected samples	No field collected samples were used in this study
Ethics oversight	Use of these animals is in compliance with ethical regulations and has been approved from the Prefecture de Police and Direction departementale des services veterinaires de Paris.

Note that full information on the approval of the study protocol must also be provided in the manuscript.